Available online at www.sciencedirect.com
ScienceDirect
Trans. Nonferrous Met. Soc. China 33(2023) 1−24
Transactions of Nonferrous Metals Society of China
www.tnmsc.cn

Additive manufacturing of high-entropy alloy composites: A review

Hamza OSMAN[1,2], Lin LIU[1]

1. State Key Lab for Materials Processing and Die & Mold Technology, School of Materials Science and Engineering, Huazhong University of Science and Technology, Wuhan 430074, China;
2. Department of Mining and Petroleum, Faculty of Engineering, Al Azhar University, Qena, Egypt

Received 26 December 2021; accepted 8 April 2022

Abstract: High entropy alloy composites (HEACs) are a new class of metal matrix composites involving a second phase, such as carbides, borides, and nitrides in high entropy alloy matrices. In recent years, HEACs have attracted wide attention due to their outstanding properties. However, the preparation of HEACs encounters great challenges when using conventional casting approaches due to serious composition segregation. 3D printing techniques solved this problem and produced components with complex geometry. Therefore, 3D printing techniques have been applied to fabricating HEAC components, and a few works on this topic have been published. To accommodate the rapid development of 3D printing of HEACs, we present a state-of-the-art overview of the recent progress of HEAC 3D printing. The article begins with an introduction of HEAs and 3D-printed HEACs. The processes of HEAC powders development, including gas atomization and mechanical alloying, are presented. The 3D printing processes of HEAC powders, such as powder bed fusion and directed metal deposition, and their microstructures are discussed. The mechanical properties of 3D-printed HEACs are discussed and compared with 3D-printed HEAs and their casting counterparts, and their hardness, resistance to wear, corrosion, and oxidation are discussed. Finally, new perspectives are outlined for future research.

Key words: high-entropy alloy; composite; additive manufacturing; reinforcement phase; microstructure; mechanical properties

1 Introduction

High entropy alloys (HEAs) are alloys that have at least 5 principal metallic elements, and each element has an atomic percentage ranging from 5% to 35% in an equimolar or near equimolar ratio [1−5]. These alloys have unique mechanical, chemical, and physical properties compared to traditional alloys, such as a combination of high yield strength and ductility [6−8], hardness [9], and strong resistance to wear [10−12], fatigue [13,14], corrosion [15], and oxidation [16,17]. Due to their high configurational entropy, HEAs form four different crystal structures of solid solution: face-centered cubic (FCC) [18,19], body-centered cubic (BCC) [20,21], hexagonal closed packed (HCP) [22,23], and eutectic mixture [24,25]. A single-phase solid solution is desirable in HEAs for achieving specific properties; for example, HEAs that form FCC structures have excellent plasticity and fracture toughness at cryogenic temperatures [26−28], but the yield strength is low, which is incompatible with industrial requirements and limits the development and applications of HEAs [29]. To further enhance the mechanical properties of HEAs, three main strategies have been introduced [30]. The first strategy is the mechanical

Corresponding author: Hamza OSMAN, E-mail: eng_hamza10@yahoo.com, hamza10@hust.edu.cn
DOI: 10.1016/S1003-6326(22)66086-2

processing, where the mechanical properties increase with decreasing the temperature due to the effect of solution, twinning, and work hardening [26]. The second strategy involves changing the chemical composition of the HEAs by adding alloying elements such as Al, Ti, W, Si, Mo, Cu, V, Nb and B [8,28,31−39]. In this case, the mechanical properties can be improved due to the phase changes that lead to additional obstacles for dislocation slip. The third strategy involves dispersion strengthening by inserting a second phase into the HEA matrices, such as SiC [40,41], TiC [42−45], and Al_2O_3 [46,47]. Increased yield strength was attributed to the presence of reinforcement particles in the HEA matrices, thereby refining the grains, hindering dislocation movement, and introducing the strain. According to the above strategies, the strength was improved, but the plasticity was significantly reduced and subjected to the strength–ductility trade-off effect; consequently, they are ineffective in manufacturing high-performance alloys with complex geometry. Recently, scientists have focused on additive manufacturing techniques to overcome the above challenges, in addition to fabricating HEAs with a complex geometrical structure that combines high strength and toughness. Additive manufacturing or 3D printing is a new processing approach in which complex parts composed of HEAs can be fabricated layer-by-layer based on computer-aided design (CAD) models [48,49]. Recently, many reviews have reported on the fabrication of HEAs by additive manufacturing techniques, and these reviews addressed the processes, microstructures, and mechanical properties of 3D-printed HEAs [50−57]. Despite numerous attempts that have been made on high entropy alloys using additive manufacturing techniques, the mechanical properties are still weak, which creates a hurdle for practical applications of HEAs. Thus, reinforcing the matrices of the HEAs by dispersion of the ceramic particles during the 3D printing process can be used. To date, a few review works about the publications of 3D-printed HEA composites (HEACs) have been reported. Thus, this work could be considered a critical review of the recent achievements of HEACs fabricated by the additive manufacturing technique in terms of their powder developments, 3D printing processes, micro-structures, and properties.

2 Development of HEAC powders

2.1 Preparation of powder for 3D printing processes

To fabricate 3D-printed HEAC products with high quality and excellent performance, the powders used must be of high quality because poor-quality powders lead to defects in the products, such as pores, cracks, and surface roughness. In general, to develop metal powders for 3D printing, various processes were used, such as gas atomization, water atomization, mechanical alloying, chemical reduction, chloride reduction, plasma atomization, plasma rotating electrode process, plasma spheroidization, chloride reduction, hydride−dehydride process, electrolysis process, and carbonyl process [53]. Gas atomization (GA) and mechanical alloying (MA) are the most common processes used for developing HEAC powders for 3D printing processes.

2.1.1 Gas atomization (GA)

Gas atomization allows for the production of fine metal spherical powders for 3D printing processes [58−60]. The schematic mechanism of GA is shown in Fig. 1(a) [53,61]. For example, the $(CoCrFeMnNi)_{99}C_1$ (at.%) HEA powders were prepared by GA (Fig. 1(b)). Most of the particles were nearly spherical with particle size distributions of 14.41 μm (d_{10}), 23.74 μm (d_{50}), and 39.08 μm (d_{90}), and exhibited the FCC structures [62]. Additionally, the prealloyed $FeCoCrNiC_{0.05}$ powder was prepared by GA. The sizes of the particles ranged from 9 to 85 μm with a mean particle size of 45 μm, the particles were nearly spherical and exhibited FCC structures [63−65].

2.1.2 Mechanical alloying (MA)

Compared to GA, the mechanical alloying process (MA) is a more convenient method and has been widely used for the synthesis of HEAC powders for 3D printing processes. Figures 2(a, b) show schematic illustrations of mechanical alloying (process and mechanism) [53,66]. Mechanical alloying is a process of repeated deformation, fracturing, and cold welding of powders in a high-energy ball mill. It is regarded as one of the most promising techniques used to prepare HEA powder with homogeneous microstructures with irregular-shaped particles [67−70]. The phases of the HEACs are affected by the milling parameters,

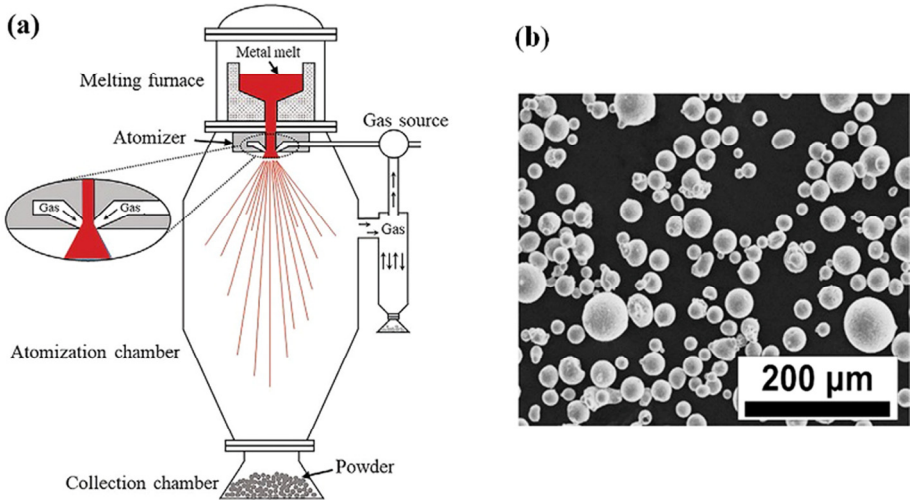

Fig. 1 Schematic illustration of mechanism of gas atomization stages (a) (Adapted with permission [53,61]) (Copyright 2020, John Wiley and Sons, and Copyright 2017, Elsevier), and morphology of gas-atomized $(CoCrFeMnNi)_{99}C_1$ HEAC powders (b) (Adapted with permission [62]) (Copyright 2019, Taylor & Francis)

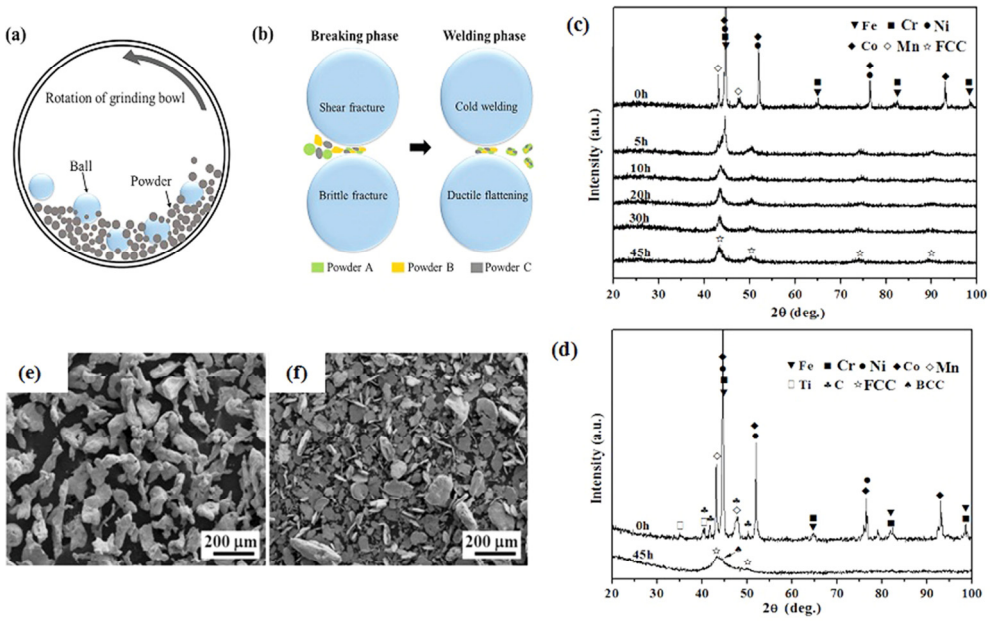

Fig. 2 Schematic representation of mechanical alloying process: Process (a) and mechanism (b) (Adapted with permission [53]) (Copyright 2020, John Wiley and Sons); XRD patterns of CoCrFeMnNi HEA powders without Ti, C (c) and CoCrFeMnNi powders with Ti, C milled for different time (d) (Adapted with permission [43]) (Copyright 2018, Elsevier); SEM images of milled CoCrFeMnNi HEA (e) and CoCrFeMnNi−TiC powders (f) (Adapted with permission [44]) (Copyright 2019, Elsevier)

such as ball-to-powder ratio, milling time, and rotating speed of the mill. For example, CHENG et al [43] studied the effect of milling time on the phases of FeCoCrNiMn powder with/without Ti and C additions. The XRD patterns of an alloyed Fe, Co, Cr, Ni, and Mn powder (without Ti and C addition) with various ball milling time are shown in Fig. 2(c). After 5 h of milling, the diffraction peak diminished, and the other peaks disappeared. After 20 h of milling, the diffraction peaks were widened, and the element peaks nearly vanished, suggesting that metal powder alloying was almost achieved. When the milling process was continued to 45 h, the diffraction peaks were widened further, the intensities of the peaks weakened, and the powders exhibited the FCC phase. The XRD of FeCoCrNiMn powders with the addition of Ti and C is shown in Fig. 2(d). Before milling, weak

diffraction peaks of Ti and C were observed with the main elements (Fe, Co, Cr, Ni, and Mn). After 45 h of milling, the alloy had a Ti and C solid solution. Furthermore, a primary FCC phase and small amounts of a BCC phase were observed, which indicated that doping with elemental Ti and C reduces the alloying process of metal powders. In addition, the CoCrFeMnNi HEA powder (99% in purity) was mixed with 5 wt.% TiC nanoparticles in a planetary ball mill at 300 r/min for 2 h. After milling, the powder exhibited irregular shapes with FCC, TiC and oxide phases (Figs. 2(e, f)) [44]. Table 1 presents the HEAC powders prepared by gas atomization and mechanical alloying with regard to the feedstock, milling parameters, and phases.

2.2 Additive manufacturing of HEACs

Additive manufacturing (AM) is a new processing technique in which the complex components of materials can be fabricated layer-by-layer based on computer-aided design (CAD) models [48,49]. The HEACs can be printed by powder bed fusion (PBF) and directed energy deposition (DED) techniques.

2.2.1 Powder bed fusion (PBF)

The powder bed fusion (PBF) process can be achieved by using an energy source, such as a laser or electron beam, to selectively melt the powder on a substrate layer by layer in a powder bed [77]. Usually, this technology is associated with metals such as titanium and plastics such as nylon [49]. In general, PBF includes the following systems: selective laser melting (SLM), direct metal laser sintering (DMLS), selective laser sintering (SLS), and electron beam melting (EBM) [78]. Selective laser melting (SLM) is one of the preferred techniques used to fabricate HEACs [29]. SLM has numerous advantages, such as a short fabrication cycle, low cost, and the ability to fabricate small and large products with complex shapes. Consequently, it is widely used in the aerospace, automotive, medical, and defense industries [79]. In addition, SLM can fabricate components with outstanding mechanical properties due to the fast cooling process. The powder bed fusion process is shown in Fig. 3.

2.2.2 Directed energy deposition (DED)

Directed energy deposition (DED), also referred to as blown powder AM or laser cladding, is the most popular printing technique used to print HEAC products. DED uses a laser, electron beam, or electric arc to melt metals in the form of powders or wires upon deposition. DED covers an array of systems, such as laser engineering net shaping (LENS), direct metal deposition (DMD), and laser metal deposition (LMD) [49,77]. The DED process is shown in Fig. 4.

PBF and DED use a high-energy source, such as a laser or electron beam, to melt metal powders

Table 1 HEAC powders developed by gas atomization and mechanical alloying with regard to feedstock, milling parameters, and phases

HEA	Second phase	Powder phase	Feed stock	Purity/%	Milling parameter			Phase	Ref.
					Ball to powder ratio	Time/h	Speed/(r·min^{-1})		
CoCrFeMnNi	C	GA	Ingot	99	−	−	−	FCC	[62]
FeCoCeNi	C	GA	Ingot	−	−	−	−	FCC	[63−65]
FeCoNiCuAl	TiC	MA	Powder	−	10:1	5	250	FCC+BCC+α-TiC	[71]
$Al_{0.5}$CoCrCuFeNi	WC	MA	Powder	−	1:1	48	250	FCC+WC	[72]
FeCoCrNiMn	SiC	MA	Powder	99.5	10:1	5−35	200	FCC+SiC	[40]
	Ti, C			99.9	15:1	5−45	250	FCC+BCC	[43]
	TiC			99.9	−	2	300	FCC+TiC+Oxides	[44]
	Al_2O_3			99.5	10:1	35	200	FCC+Al_2O_3	[46]
	TiN			−	6:1	2	150	FCC+TiN	[73]
	TiN			−	6:1	0.5−1.5	150	FCC+TiN	[74,75]
	BMG			−	−	4	400	FCC	[30]
AlCoCrFeNi	NbC	MA	Powder	99.5	8:1	2	40	FCC+BCC+NbC	[76]

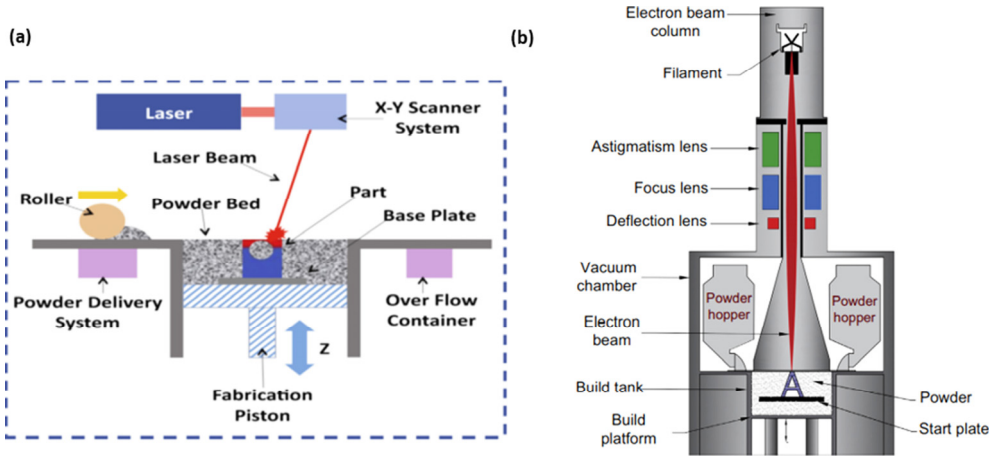

Fig. 3 Powder bed fusion process: (a) SLM; (b) EBM (Adapted with permission [80]) (Copyright 2019, Elsevier)

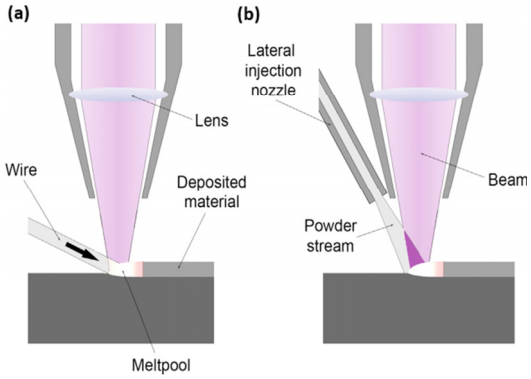

Fig. 4 Directed energy deposition technique (DED), with metal feedstock introduced to energy source in form of wire (a) or as powder (b) (Adapted with permission [49]) (Copyright 2018, Elsevier)

layer by layer with ultrafast heating/cooling rates of 10^3−10^8 K/s, resulting in refined microstructures, which is important for enhancing the properties of printed HEAC products [57, 81−83]. The difference between the PBF and DED techniques is the powder feeding method. In BPF, the powders are spread over the building podium by a blade or roller, while in the case of DED, the powders are blown from the nozzles [53].

2.2.3 Other processes

In addition to the previous processes, there are other techniques used to print HEAC products, such as the friction deposition technique, in which AA5083/CoCrFeNi HEACs were printed [84]. In addition, three-dimensional high entropy alloy−polymer composite nanolattices that overcome the strength−recoverability trade-off were fabricated via two-photon lithography and magnetron sputtering deposition [85]. To produce a CoCrFeNi HEA, a non-beam approach to the additive manufacturing of high-entropy alloys was developed based on the 3D extrusion of inks containing a blend of oxide nanopowders (Co_3O_4 + Cr_2O_3 + Fe_2O_3 + NiO), followed by co-reduction and sintering [86]. AlCoCrCuFeNi HEA particles reinforced surface MMCs on AZ91D were successfully fabricated using the laser melting injection technique (LMI) [87]. HEA particles have great potential for mechanical property enhancement compared to conventional lightweight alloys. Therefore, a novel Al matrix composite reinforced by $Al_{0.8}$CoCrFeNi HEA particles was fabricated by multi-pass friction stir processing [88].

3 Structure of 3D-printed HEA composites

This section is focused on the microstructures resulting from the additive manufacturing processes of the HEAC powders, such as PBF and DED.

3.1 3D-printed HEACs fabricated by PBF technique

3.1.1 Carbon-containing high-entropy alloys (C-HEAs)

Adding a small amount of interstitial materials, such as carbon and nitrogen, to the high-entropy alloy matrices resulted in enhanced mechanical properties because of the changes in the micro-structures and deformation mechanism [89−97]. FeCoCrNi has been studied as an HEA with a simple FCC structure and excellent mechanical properties [98]. The studies [63−65] were conducted on the effect of carbon on the FeCoCrNi HEA during the SLM process and the effect of processing parameters on the product properties. In

the first study [63], the $FeCoCrNiC_{0.05}$ HEA was fabricated using SLM at a laser power in the range of 200−400 W and scanning speed in the range of 800−2000 mm/s. Near full density was achieved when using a low laser scanning speed (800 mm/s). The density increased by increasing the power and decreasing the scanning speed. The carbon dissolved fully in the HEA, a monophase of FCC was indicated, and no carbide phase was detected. The microstructures of the top, middle, and bottom parts of the SLMed samples are shown in Fig. 5. The grains in the three different regions were randomly oriented. Equiaxed grains existed in the middle and bottom parts, while the grains in the top part were columnar, which was attributed to the temperature gradient and cooling rate.

For the second study [64], the laser power was 400 W and the scanning speed was 800 mm/s during the SLM process. Nanosized $M_{23}C_6$ carbides precipitated at the grain boundaries and dislocation networks in the $CrFeCoNiC_{0.05}$ HEA samples were produced by the SLM process (Fig. 6), which was related to high residual stress and the heating/cooling conditions.

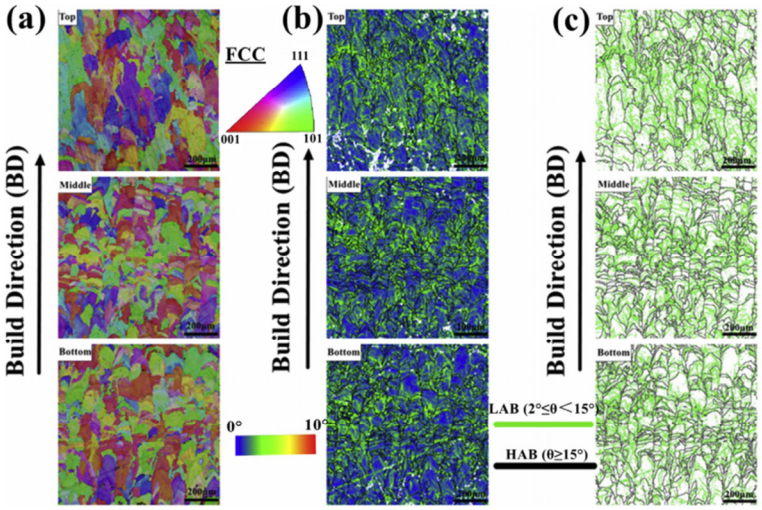

Fig. 5 EBSD of SLMed $FeCoCrNiC_{0.05}$ HEA (400 W, 800 mm/s): (a) Inverse pole figure (IPF); (b) Local misorientation (LM) maps; (c) Grain boundaries (GB) maps of $FeCoCrNiC_{0.05}$ (Adapted with permission [63]) (Copyright 2018, Elsevier)

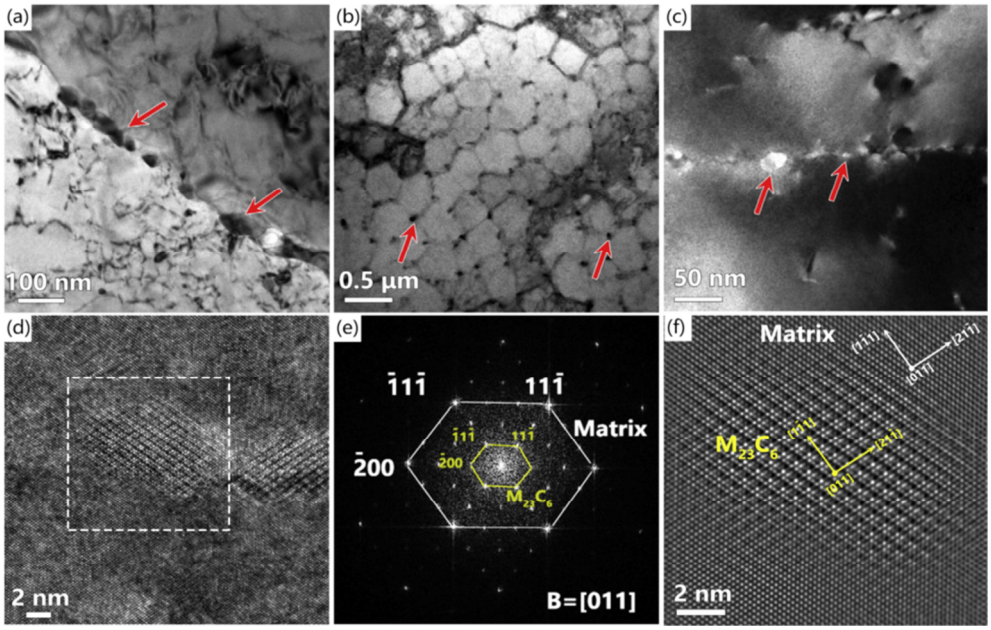

Fig. 6 TEM images of precipitates at grain boundary (a), cellular (b) and columnar subgrain boundaries (c), respectively, HRTEM image of nanosized carbides (d) at columnar boundary in (c) and FFT pattern (e) and Fourier filtered image (f) of selected square region in (d) (Adapted with permission [64]) (Copyright 2018, Elsevier)

In the last study [65], the $FeCoCrNiC_{0.05}$ HEA was fabricated at a laser power of 400 W and a scanning speed of 800 mm/s followed by annealing at 1073 K for different time. Under annealing conditions for different time, the grains were equiaxed and randomly oriented. With the prolongation of annealing time, the size of grains remained obviously unchanged (approximately 40−50 μm), and nanoscale $Cr_{23}C_6$ carbides precipitated at the boundaries of grains or cell structures of $FeCoCrNiC_{0.05}$ produced by the SLM process (Fig. 7).

PARK et al [62] fabricated $(CoCrFeMnNi)_{99}C_1$ HEA by SLM using 90 W laser power and scanning speeds of 200 (C-HEA-V200) and 600 mm/s (C-HEA-V600). C-HEA-V200 sample exhibited a large columnar grain structure with an average size of ~35.5 μm, while mixed columnar and equiaxed grain structures with an average size of ~20.3 μm were observed in the C-HEA-V600 sample. This was attributed to the difference in the heat input during the SLM process at different scanning speeds. Additionally, subgrain boundaries were made of dislocation networks decorated by nanosized $M_{23}C_6$ carbides, as shown in Fig. 8, which was related to the heating/cooling conditions of the SLM process.

Near-fully dense HEA, $Fe_{49.5}Mn_{30}Co_{10}Cr_{10}C_{0.5}$ (at.%), with excellent mechanical properties was additively manufactured using SLM by ZHU et al [99], where P=180 W and v=1000 mm/s. The SLMed sample consisted of an FCC structure without carbides. Additionally, a hierarchical microstructure comprising equiaxed grains and a columnar structure was observed (Fig. 9). This hierarchically heterogeneous microstructure was formed because of the rapid melting/solidification during SLM, which resulted from the printing parameters.

3.1.2 HEAs with ceramic particles

TiN reinforcement particles have high strength, high melting temperature of 2950 °C, and high thermodynamic stability without the phase transformations [100]. According to these properties, LI et al [73,74] reinforced the matrix of FeCoCrNiMn HEA by nano-TiN particles using SLM. The microstructure of the HEA produced by SLM without TiN exhibited a strong texture along the building direction, and the grains grew toward the building direction, forming elongated grains (Figs. 10(a, b)), while the HEA+TiN composite produced by SLM exhibited reinforcement particles of TiN distributed at the grain boundaries of the HEA matrix with refined grains and the absence of the texture (Fig. 10(c)). This was attributed to the wettability between HEAs and TiN particles, which worked as nucleation points in assisting the heterogeneous nucleation for the FCC phase; eventually, this led to the refinement of the grains, which grew to isotropic and equiaxial grains [43].

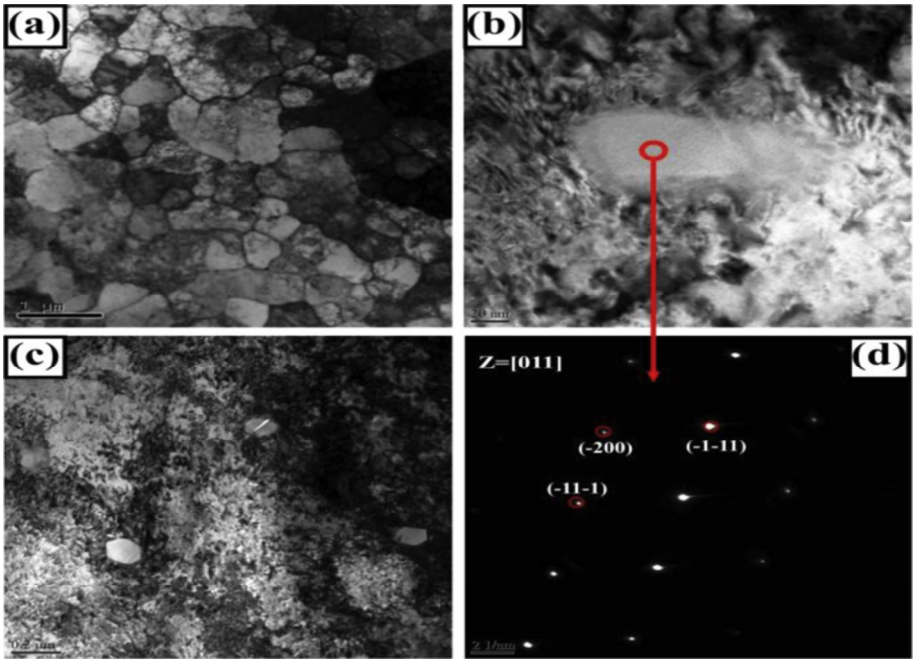

Fig. 7 TEM images of annealed $FeCoCrNiC_{0.05}$ HEA at 1073 K for 0 h (a), 0.5 h (b), 8 h (c), and selected area diffraction pattern (d) (Adapted with permission [65]) (Copyright 2019, Elsevier)

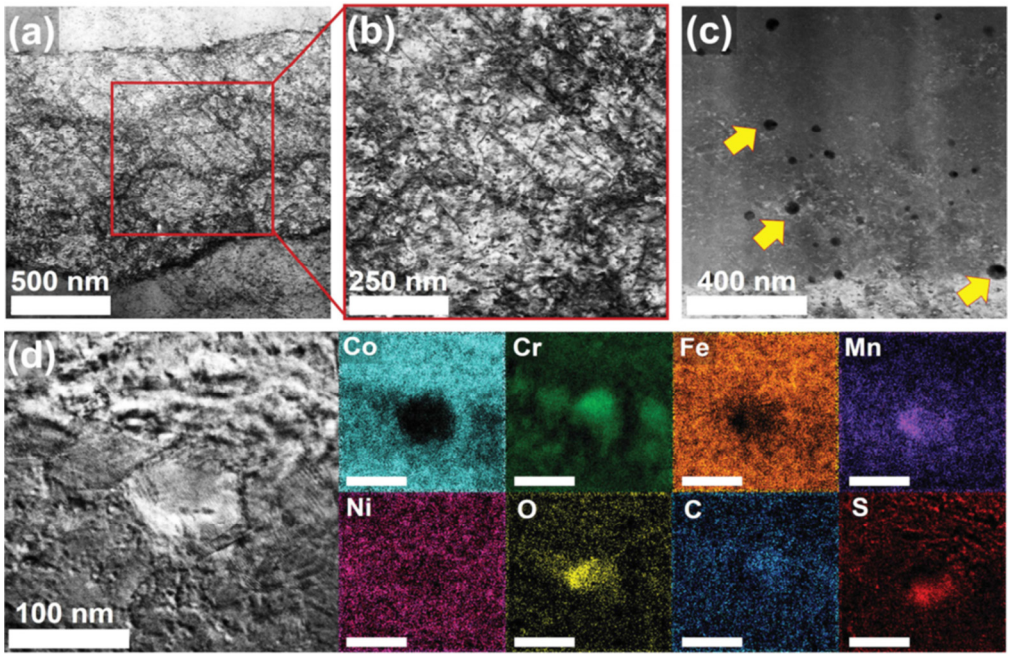

Fig. 8 TEM images of SLMed C-HEA at 200 mm/s scanning speed: (a) Bright-field image of cellular structures; (b) Magnified image; (c) STEM image showing nano-precipitates; (d) EELS mapping images of substitutional (Co, Cr, Fe, Mn, and Ni) and interstitial (O, C, and S) elements for nano-precipitates (Adapted with permission [62]) (Copyright 2015, Taylor & Francis)

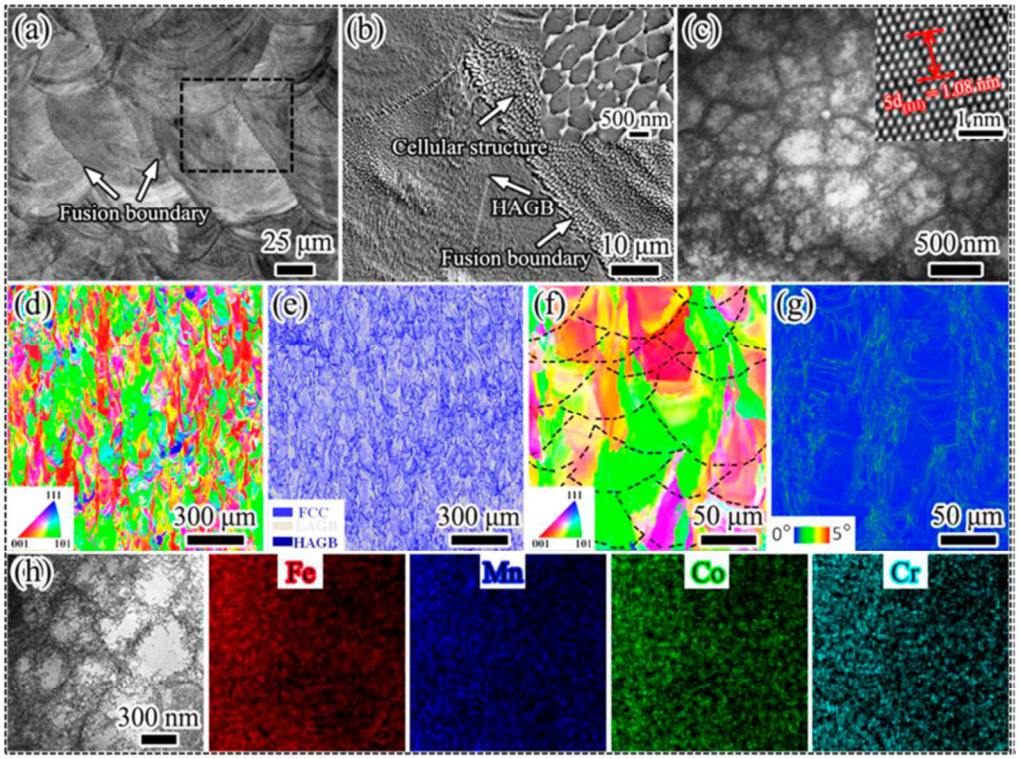

Fig. 9 OM images of SLMed HEA (a), SE image taken from area in (a) with inset indicating equiaxed cellular structures (b), STEM micrograph of equiaxed cellular structures with inset HRTEM image revealing distance across 5 planes (c), IPF map (d), phase map superimposed with GB map (e), IPF (f) and KAM (g) maps (the dashed lines in (f) show the fusion boundaries), and STEM−EDS maps of cellular structures (h) (Adapted with permission [99]) (Copyright 2019, Taylor & Francis)

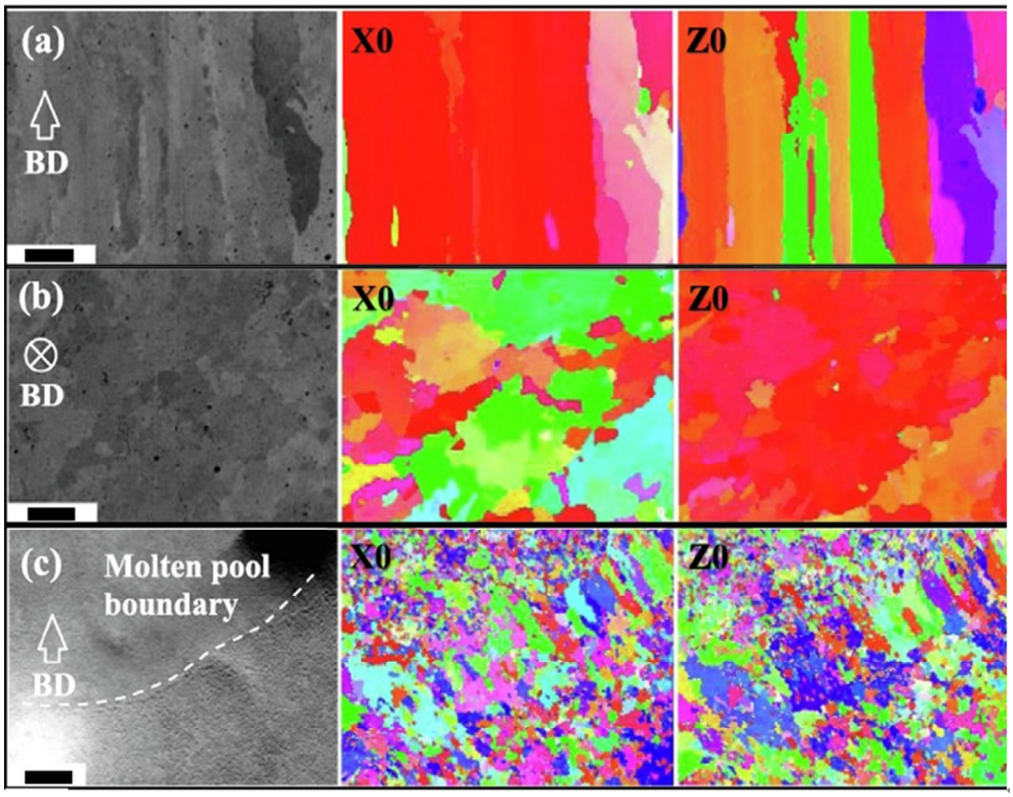

Fig. 10 IPF-X, IPF-Z and IPF images of printed HEA parallel to building direction (BD) (a), and perpendicular to BD (b); IPF-X, IPF-Z and IPF images of printed TiN/HEA parallel to BD (c) (Adapted with permission [73]) (Copyright 2019, Elsevier)

Another study was conducted by LI et al [75], where 5 wt.% TiN nanoparticle reinforced CoCrFeMnNi matrix was fabricated using the SLM process and remelting laser scan strategy (RLSS). Because of the RLSS, a more equal TiN particle distribution was observed, and much finer and equiaxed HEA grains were obtained. This study also focused on obtaining a novel ultrafine-grained and hybrid amorphous crystalline structure, as shown in Fig. 11. The additive TiN particles improved the entropy at elevated temperatures and lowered the Gibbs free energy of the solid solution phase of HEA composite. These two mechanisms resulted in the formation of the amorphous phase.

Fe-based metallic glasses (MGs) have an excellent strength of approximately 3 GPa due to their disordered atomic structure and their similar chemical composition with FeCoCrNiMn HEA [101]. For these reasons, LI et al [30] designed and fabricated high entropy alloy/metallic glass composites by SLM. In addition to the amorphous phase, two different high entropy phases were observed in the HEA/MG composite interfacial region, as illustrated in Fig. 12. This was attributed to the small atomic size difference between the FeCoCrNiMn HEA and the FeCoCrMoCBY amorphous alloy.

Because of the multicomponent solid solution, HEAs have excellent mechanical properties with great structural and thermal stability without phase changes. For these reasons, HEAs can be used as reinforcement and bender phases [102]. LI et al [103] used 20 wt.% AlCoCrFeNiCu HEA as a binder to fabricate solid block cemented tungsten carbide samples by SLM. In general, the chemical compositions and microstructures varied along the building direction, which was affected by the dilution effect generated by elemental diffusion from the substrate and the element evaporation produced by the high-power laser. At the lower part of the sample, the W_2C dendrite was formed, followed by the FCC phase because of the rapid cooling of the remaining melt pools. At the upper part of the sample, due to the repeated heating of the W_2C/HEA dendritic structure by using laser continuity, coarser WC and η-carbide precipitates were obtained.

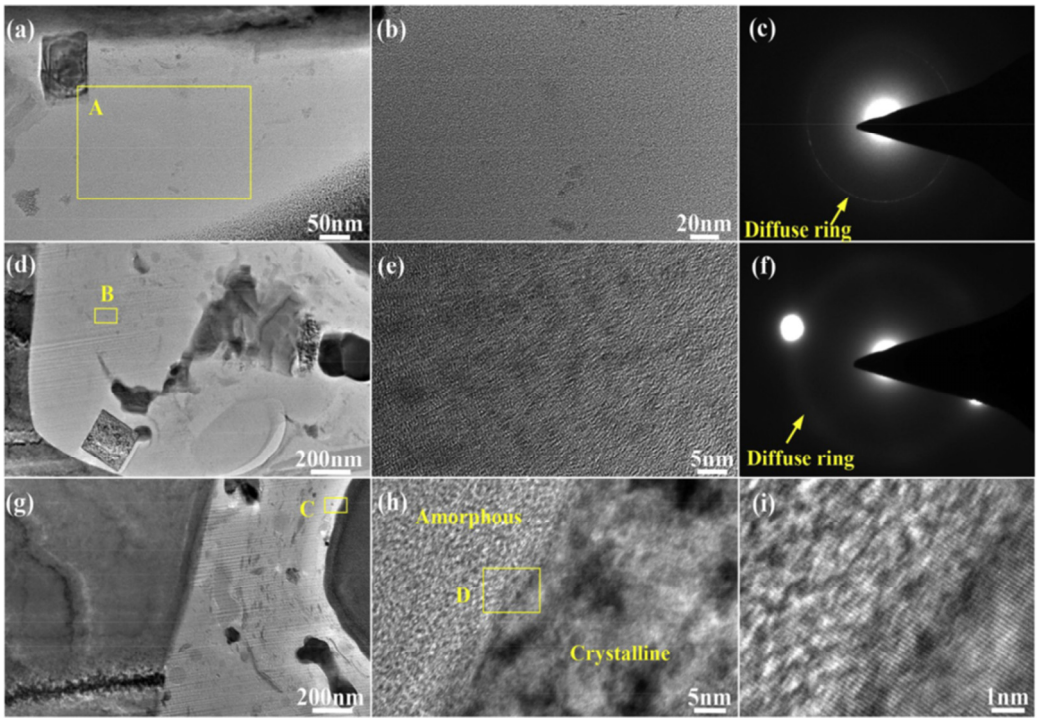

Fig. 11 TEM micrograph of RLSS−SLMed TiN/HEA composite: Amorphous micro-region (a), with enlargement at Region A (b), and its SAED pattern (c); Composite micro-region (d), with enlargement at Region B (e), and its SAED pattern (f); Another composite micro-region (g), with enlargements at Region C (h), and D (i) (Adapted with permission [75]) (Copyright 2020, Elsevier)

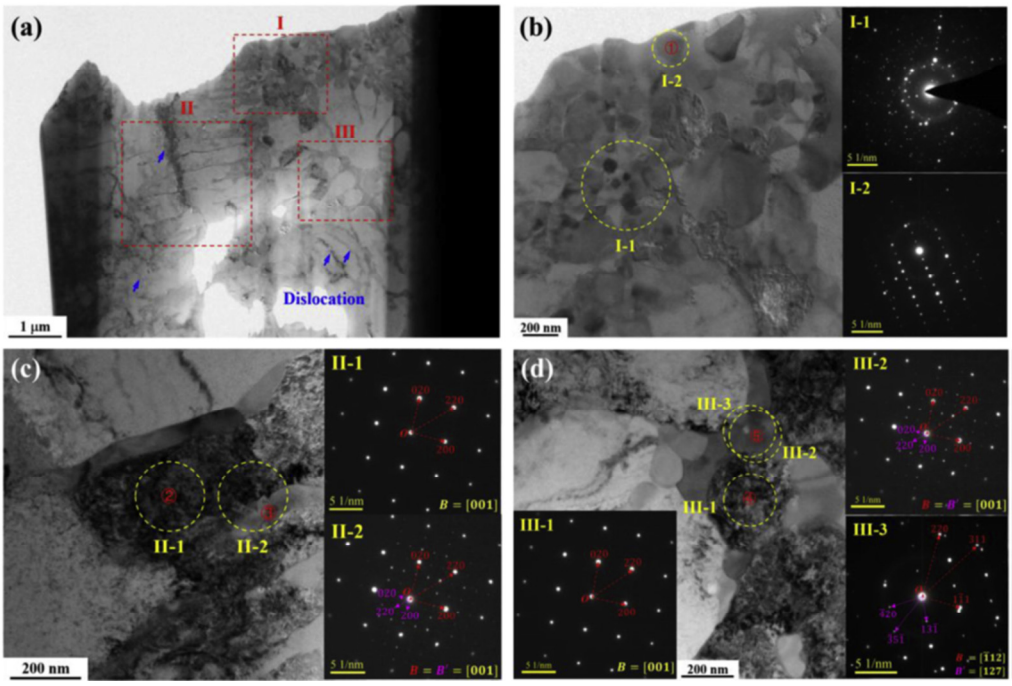

Fig. 12 TEM bright field image of interfacial zone divided into three regions (I, II, III) (a); Bright field image of Region I (Zone I-1 shows multi-crystal feature, and Zone I-2 reveals nanocrystals $FeMo_2$ phase) (b); Bright field image of Region II (Zone II-1 reveals FCC crystal, while the diffraction pattern in Zone II-2 shows two different crystals) (c); Bright field image of Region III, clarifying two different crystals (d) (Adapted with permission [30]) (Copyright 2020, Elsevier)

3.2 3D-printed HEACs fabricated by DED technique

LI et al [104] prepared CrMnFeCoNi+WC composite by the LMD process. After the addition of the WC particles, fine microstructures were obtained without any pores or cracks, and $M_{23}C_6$ carbides precipitated. These precipitates act as heterogeneous nucleation sites during the solidification process, leading to finer grain size distributions. In addition, they potentially strengthen the matrix by hindering and deflecting the slip bands. WELK et al [105] studied the glass forming ability of two bulk metallic glass and high entropy alloy composite systems (HEA/BMG) fabricated by LENS^{TM}. The first deposition (from $Zr_{57}Ti_5Al_{10}Cu_{20}Ni_8$ to $CoCrFeNiCu_{0.5}$) was deposited at a laser power of 250 W and scanning speed of 8 mm/s. The second deposition (TiZrCuNb to $(TiZrCuNb)_{65}Ni_{35}$) was deposited at a laser power of 295 W and scanning speed of 8 mm/s. A fully amorphous region in the first gradient was observed, while amorphous matrix/crystalline dendrite composite structures were detected in the second gradient. The glass-forming ability in the HEAs leads to new alloys with enhanced mechanical properties. Ultrafine nanocrystals (UNs) modified HEACs were fabricated by LMD of the yttria partially stabilized ZrO_2 (YPSZ) and the FeCoCrAlCu mixed powders on the aviation turbine blade fabricated of the additive manufacturing TC17 titanium alloy [106]. HEACs exhibited fine microstructures free of microcracks, and many $AlCu_2Zr$ UNs were produced in the HEACs matrix (Fig. 13(a)). The mechanism for the formation of $AlCu_2Zr$ in-situ intermetallics by LMD of the Al, Cu and Zr free-state particles in the laser-induced molten pool was proposed (Figs. 13(b, c)). Cu was difficult to dissolve with the other elements in FeCoCrAlCu due to the high mixing enthalpies between Cu and other elements, promoting the formation of $AlCu_2Zr$ UNs. The nanoscale *I*-phase with fivefold symmetry was obtained, as shown in Fig. 13(d), which is due to the thermodynamic driving free energy and the kinetics of quasicrystalline phase formation relative to the solidification rates. Moreover, lattice distortion in the *I*-phase was detected due to the high diffusion of UNs and the ultrafine microstructure. The UNs were able to ruin the atomic equilibrium state, increasing the free energy and creating lattice distortions in the *I*-phase.

By adding SiB_2, as shown in Fig. 14, many nanorods were formed, and the detained UNs could be easily reunited due to the surface effect, retarding the growth of the nanorods to a certain extent [106].

3D-printed HEACs are very promising materials with excellent mechanical properties. Therefore, HEACs are used as coatings to improve the surface properties of printed products against tough environmental conditions. For example, a Q235 steel substrate coated by $AlCoCrFeNi_xNbC$ HEAC coatings was prepared via laser cladding by LI et al [76]. The AlCoCrFeNi HEA exhibited a mixture of simple BCC and FCC structure phases, and the microstructure had many elongated, blocky and few equiaxed grains. The addition of NbC particles resulted in a decrease in the FCC phase, and NbC particles were mainly distributed andprecipitated at the grain boundary of the HEAs. Additionally, the grains were elongated, and their growth direction was changed, and the NbC particles inhibited HEA grain growth due to a strong pinning effect. In situ TiN particle-reinforced

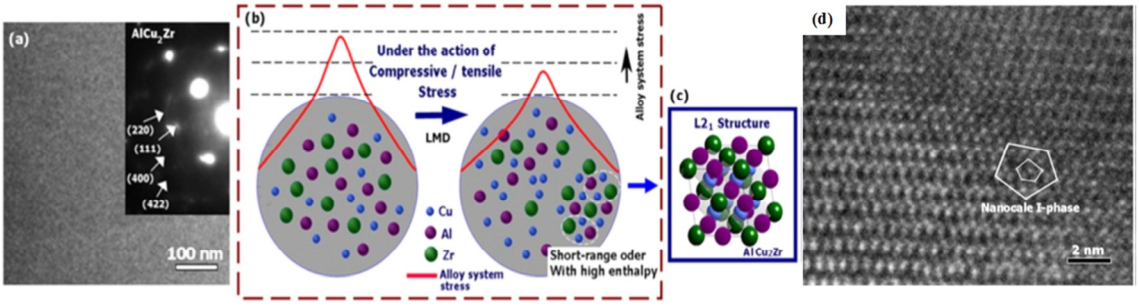

Fig. 13 Analysis of HEACs: (a) Twin crystals and amorphous, HRTEM micrograph and corresponding SAED pattern; (b, c) Schematic illustration of formation of $AlCu_2Zr$ UNs; (d) Nanoscaled *I*-phase (Adapted with permission [106]) (Copyright 2017, Elsevier)

$CoCr_2FeNiTi_x$ HEA coatings were fabricated using laser cladding on 904L stainless steel by GUO et al [107]. The results revealed that the structures of coatings consisted of FCC, TiN, and a few Laves phases. Without adding Ti, microstructure of coating was columnar crystals, while after adding Ti, the coating was composed of irregular dendrites, granular TiN ceramics, and few Laves phases. CNT-reinforced HEACs were produced on TA2 titanium alloy using LMD of FeCoCrAlCu−(nano-SiB_6)−(Ni/Ag coated CNTs) mixed powders by LI et al [108]. Figure 15 shows schematic diagrams of the laser viscose and diffusion mechanism under the influence of the laser pool at high temperature. Large quantities of the photons entered the laser pool from the laser beam during the LMD process, surrounding atoms with photons, which hindered the motions of the atoms, as indicated in Fig. 15(a). Figure 15(b) shows that the UNs were able to obtain sufficient energy from the

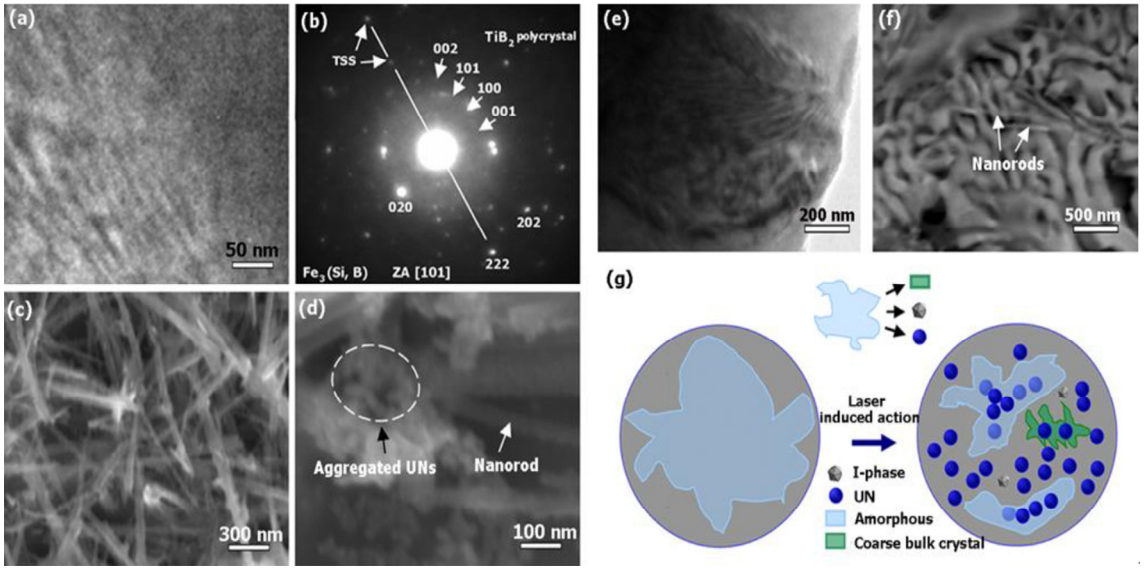

Fig. 14 Analysis for $FeCoCrAlCu/SiB_2$ HEACs: (a) HRTEM test location; (b) Corresponding electron diffraction pattern; (c, d) SEM micrographs of nanorods, and aggregated UNs and nanorods; (e) HRTEM test location; (f) SEM micrograph of eutectics; (g) Schematic illustration of decomposition of amorphous under action of laser beam (Adapted with permission [106]) (Copyright 2017, Elsevier)

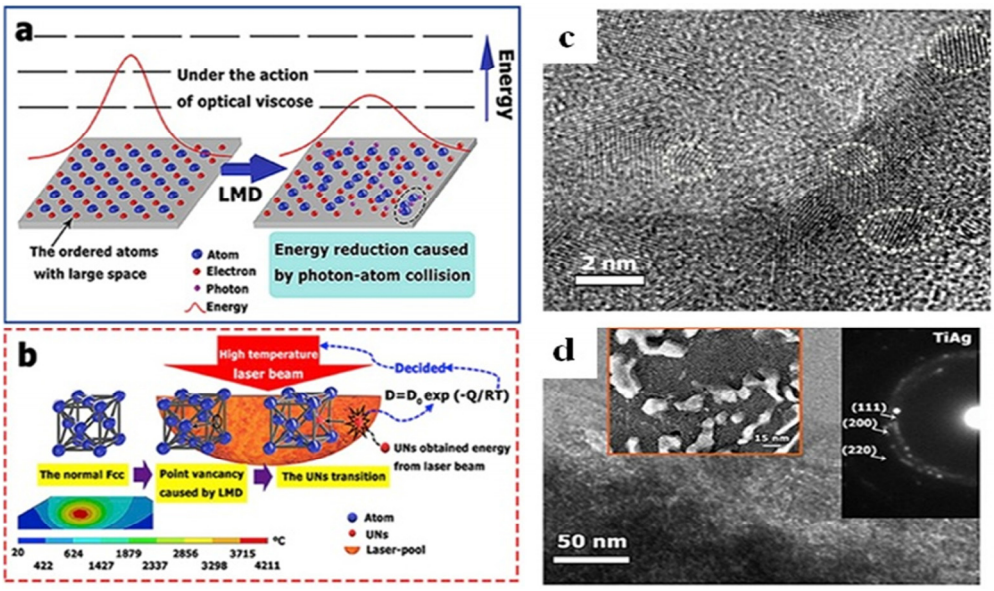

Fig. 15 Schematic diagrams of laser viscose (a), diffusion mechanism under action of laser-pool with high temperature (b); HRTEM micrograph of HEACs (c), and SAED pattern of TiAg phase and UNs of HEACs (d) (Adapted with permission [108]) (Copyright 2020, Elsevier)

laser beam such that a portion of UNs penetrated into the originally ordered atom arrangement, resulting in lattice distortion due to the actions of the high diffusion rate and the ultrafine microstructure of UNs. In addition, during the tunneling of UNs, enormous energy was released into the laser pool, which was beneficial to the complete diffusion of UNs. Figure 15(c) reveals that a large number of lattice fringes of the nanocrystals were formed, and lattice distortions were formed near them. The fact that the production of nanocrystals caused the fusion point of the laser pool to be reduced, as well as the high interface energy of UNs, became the driving force of the atomic arrangement movements, promoting the formation of a compact/fine microstructure. As illustrated in Fig. 15(d), the SAED pattern of HEACs exhibited that the TiAg nanoscale phase grew along the (111), (200) and (220) planes, showing that these amorphous phases would crystallize, but the laser pool solidification process was completed, promoting UNs to be produced.

LI et al [109] deposited FeCoCrAlCu−$MoSi_2$−Mn−Sb powders on a T6 Ce/Er-modified hot-rolled Al−Mg−Si−Cu alloy substrate using the LMD technique. Amorphous/nanocrystalline HEACs were observed. Many Co_3Mo_2Si UNs were produced that grew along the (101), (103), (112) and (213) planes. The amorphous phases were limited to grow up during the crystallization growth process, hindered by the UNs, promoting the formation of HEACs with a fine microstructure. Table 2 presents a summary of the microstructures observed in various HEAC products manufactured by AM technology.

4 Properties of 3D-printed HEACs

3D-printed HEACs are very promising materials with excellent properties because of the addition of reinforcement particles. These particles distributed and precipitated at the grain boundary of HEAs, inhibiting HEA grain growth; thus, the properties were improved.

4.1 Mechanical properties

For C-HEAs, ZHOU et al [63] studied the effect of the SLM process parameters on the tensile properties, as shown in Fig. 16(a). They found that the addition of carbon led to further improvement of the strength (yield strength of 656 MPa, and tensile strength of 797 MPa), which could be mainly due to solid solution strengthening caused by adding carbon. Fine microstructures, resulting from submicron solidification of the cellular structure and SLM sample grain refinement, also promoted the yield strength. They also observed that the elongation exhibited a significant difference, which may be attributed to the defects in the specimens, such as porosities and micro-cracks resulting from the effects of the printing parameters. Consequently, a convenient combination of processing parameters, such as scanning speed and laser power, was important to obtain better mechanical properties of $FeCoCrNiC_{0.05}$ fabricated via SLM. The effects of the annealing process at 1073 K for 0.5 and 8 h on the mechanical properties of $FeCoCrNiC_{0.05}$ were discussed by ZHOU et al [65]. The results showed that the annealing treatment could lead to an increase in the yield and tensile strength, but a decrease in elongation. According to Fig. 16(b), the SLMed $FeCoCrNiC_{0.05}$ annealed for 0.5 h had the highest yield strength (787 MPa), but when the annealing time increased to 8 h, the yield strength decreased (720 MPa). The explanation for this is shown in Fig. 16(c), which clarified the estimated strength contribution from solid solution hardening and precipitation hardening. The precipitation hardening increased sharply at 0.5 h annealing time, while the solid solution hardening decreased slightly. When the annealing duration was extended to 8 h, the precipitation hardening increased slightly, but the solid solution hardening decreased. As a result, the yield strength decreased. PARK et al [62] compared the mechanical properties of 1%C−CoCrFeMnNi HEA additively manufactured using selective laser melting compared to its casting counterparts (Fig. 16(d)). It was noted that the yield strength of the SLMed CoCrFeMnNi HEA was higher than that of the casting C-HEA. Furthermore, superior tensile properties of the SLMed 1%C−CoCrFeMnNi HEAs were achieved compared to pure and as-cast CoCrFeMnNi HEAs. This was attributed to their complicated microstructure with a combination of various strengthening mechanisms (i.e., solid solution, grain refinement, dislocation density, and nanoprecipitation), which were achieved by the addition of a small amount of carbon with different energy inputs.

Table 2 Summary of microstructures observed in various HEAC products manufactured by AM

HEA	Second phase	Printing process	Parameter		Microstructure	Ref.
			P/W	v/(mm·s^{-1})		
FeCoCrNi		SLM	200−400	800−2000	Monophase of FCC, with carbon dissolving in HEA, and no carbide phase detected	[63]
	C	SLM	400	800	Nano-sized $M_{23}C_6$ carbides precipitating at grain boundaries and dislocation networks	[64]
		SLM and annealed at 1073 K for 0.5 h	400	800	Equiaxed and randomly grains with size about 40−50 μm and $Cr_{23}C_6$ carbides precipitating on boundaries of grains or cell structures	[65]
$Fe_{49.5}Mn_{30}Co_{10}Cr_{10}$	C	SLM	180	1000	FCC structure without carbides and hierarchical microstructure comprising equiaxed grains and columnar structure	[99]
CoCrFeMnNi	C	SLM	90	200, 600	Mixed columnar and equiaxed grain structures and subgrain boundaries made of dislocation networks decorated by nanosized $M_{23}C_6$ carbides	[62]
	BMG	SLM	185	600	Amorphous phase, and two different high entropy phases at high entropy alloy/metallic glass interfacial region	[30]
	TiN	SLM	250	450	Reinforcement particles of TiN distributing at grain boundaries of HEA matrix with refined grains and absence of texture	[73]
	TiN	SLM−RLSS	375	1600	Much finer and equiaxed HEA grains and more evenly TiN particle-distribution with novel ultrafine-grained and hybrid amorphous/crystalline structure	[75]
	WC	LMD	1000	8.3	Fine microstructures without any pores or cracks and precipitates of $M_{23}C_6$	[104]
AlCoCrFeNiCu	WC	SLM	140	90	At lower part of sample, W_2C dendrite, and interdendritic FCC phase; At upper part of sample, coarser WC and η-carbide precipitates	[103]
FeCoCrAlCu	ZrO_2	LMD	100−2500	4−20	Fine microstructure free of micro-crack and $AlCu_2Zr$ UNs attached to HEACs matrix	[106]
FeCoCrAlCu	$MoSi_2$−Mn−Sb	LMD	1000−3000	1−15	Amorphous/nanocrystalline HEACs and lots of Co_3Mo_2Si UNs growing along (101), (103), (112) and (213) planes	[109]
AlCoCrFeNi$_x$	NbC	Laser cladding	2500	3	FCC phase and NbC particles distributing and precipitating at elongated grain boundary of HEAs	[76]
$CoCr_2FeNiTi_x$	TiN	Laser cladding	1800	7	FCC and irregular dendritic, granular TiN ceramics, and a few Laves phases	[107]

Titanium carbide (TiC) is one of the ceramic reinforcement particles, that is an excellent reinforcer due to its excellent elastic modulus, high hardness, low density, high melting temperature, thermodynamic stability, and good wettability without undergoing phase transformation [110]. AMAR et al [111] improved the mechanical properties of the CoCrFeMnNi HEA using LMD by the addition of TiC (0, 2.5, and 5 wt.%). By increasing the added TiC, the yield and ultimate tensile strength increased, and the elongation decreased. At 0 wt.% TiC, the yield strength and tensile strength were approximately 300 MPa and 550 MPa, respectively, and the elongation was over 50%. At 2.5 and 5 wt.% TiC, the yield stress was remarkably improved (330 MPa and 385 MPa, respectively), the tensile strength (610 MPa and 723 MPa, respectively) and the plasticity decreased to 47% and 32%, respectively, as shown in Fig. 17(a). To understand the influence of the addition of TiC on the deformation modes, the fractography of LMDed CrMnFeCoNi with

different TiC additions was examined, as shown in Fig. 17(b). The necking deformation was observed on the fractured samples without TiC addition (Fig. 17(a′)) and was not observed by adding 2.5 and 5 wt.% TiC (Figs.17(d′, g′)). Furthermore, as shown in Figs. 17(b, c), there was a dense population of deep dimples at the fractured surface and many slip bands on the side surface, demonstrating that the deformed LMD samples had high uniform plastic deformation prior to fracture. With 2.5 wt.% TiC, the deep dimples became shallow dimples (Figs. 17(e′, f′)) and finally

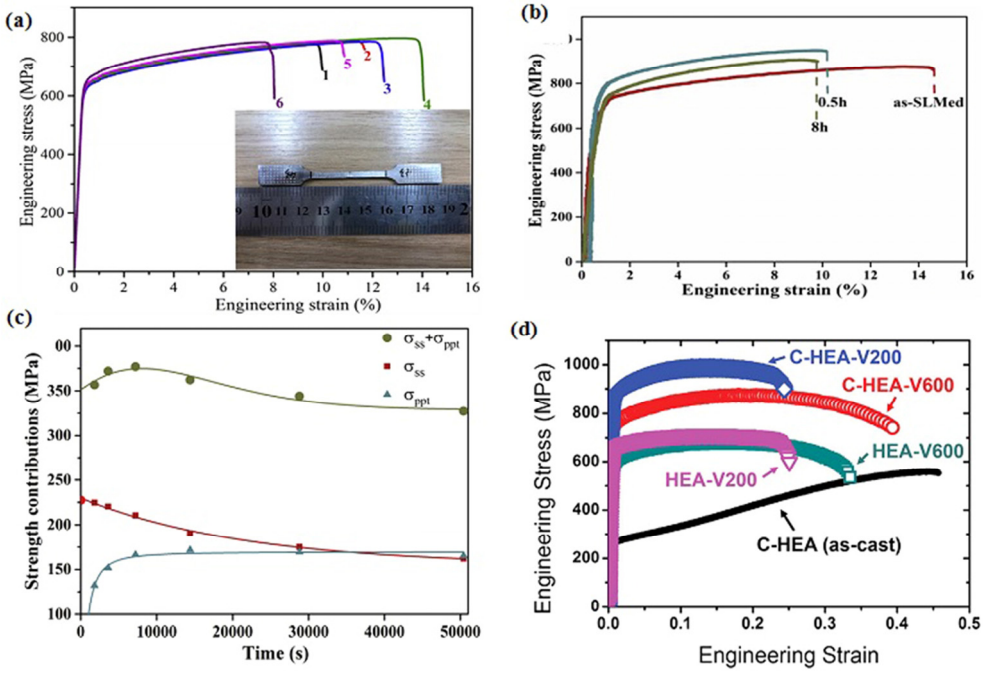

Fig. 16 Room-temperature tensile strain−stress curves for $FeCoCrNiC_{0.05}$ alloys (a) (Adapted with permission [63]) (Copyright 2018, Elsevier); Typical engineering stress−strain curves of SLMed and annealed $FeCoCrNiC_{0.05}$ (1073 K for 0.5 h and 8 h) (b) (Adapted with permission [65]) (Copyright 2019, Elsevier); Strength contributions from different hardening mechanisms (c) (Adapted with permission [65]) (Copyright 2019, Elsevier); Tensile properties of as-cast and SLMed of CoCrFeMnNi and $(CoCrFeMnNi)_{99}C_1$ (d) (Adapted with permission [62]) (Copyright 2019, Taylor & Francis)

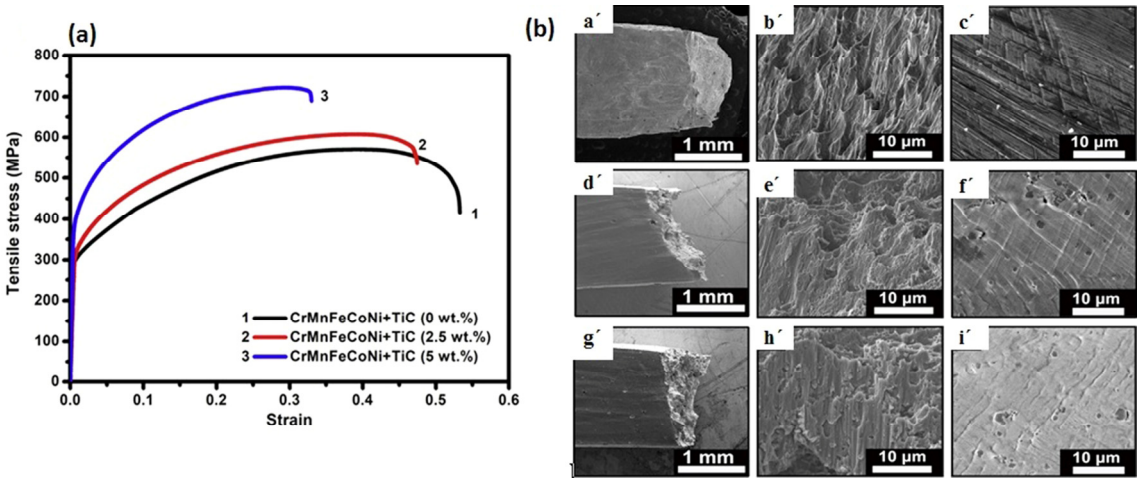

Fig. 17 Tensile curves of LMDed CrMnFeCoNi HEAs with different TiC additions (0, 2.5, and 5 wt.%) at room temperature (a) and fractographs of LMDed CrMnFeCoNi with different TiC additions (b) (Overall appearances of fractured sample with TiC additions of 0 wt.% (a′), 2.5 wt.% (d′) and 5 wt.% (g′), fractographs of sample with TiC additions of 0 wt.% (b′), 2.5 wt.% (e′) and 5 wt.% (h′) and side surface of fractured sample with TiC additions of 0 wt.% (c′), 2.5 wt.% (f ′) and 5 wt.% (i′)) (Adapted with permission [111]) (Copyright 2019, Elsevier)

disappeared upon adding 5 wt.% TiC (Figs. 17(h′, i′)). In addition, the number of slip bands decreased with increasing TiC addition, as shown in Figs. 17(c′, f, i′). In conclusion, the addition of the TiC particles strengthened the HEA matrix by hindering and deflecting the slip bands.

Additionally, the tensile properties of LMDed CrMnFeCoNi HEA fabricated by adding WC were improved. At room temperature, the addition of WC (5 and 10 wt.%) enhanced the yield strength from 300 to 502 and 675 MPa, the tensile strength from 550 to 776 and 845 MPa, and the plasticity decreased from 50% to 37% and 9%, respectively. At 873 K, the addition of 5 wt.% WC also improved the tensile strength from 280 to 405 MPa, with a relatively small decrease in plasticity from 57% to 45%. This was due to the combined effects of grain refinement and precipitate reinforcement [104].

The compressive properties and fracture toughness of FeCoCrNiMn/Fe-based MG composite (from 0 to 30 wt.%) fabricated by SLM are shown in Figs. 18(a, b), respectively. When the fraction of amorphous powder was between 5 and 20 wt.%, the composites exhibited excellent strength (916−1517 MPa) and high fracture toughness (65.67−126 MPa·m$^{1/2}$). In this case, with increasing Fe-based amorphous alloy content, the HEACs strength increased up to 1517 MPa, while the ductility and toughness decreased, including the fracture toughness, which decreased continuously to 65.67 MPa·m$^{1/2}$ by mixing 20 wt.% amorphous alloy. This was attributed to the reinforcement particles that hindered the movements of the dislocation. By increasing the added reinforcement particles to 30 wt.%, the FeCoCrNiMn/Fe-based MG composite samples were broken during the test, exhibiting brittle features. This was because of the excess amorphous particles, which resulted in microcracks in the composite during the SLM process due to the stress concentration [30].

The HEA/A5083 composite fabricated by the friction deposition technique exhibited excellent tensile and compressive strengths compared to the standard wrought alloy AA5083 H112 [112] and exhibited a much better combination of strength and ductility than the conventional aluminum matrix reinforced with ceramic particles. This was a result of the nanocrystalline CoCrFeNi HEA reinforcement particles, with a uniform distribution in the ultrafine-grained aluminum matrix [84].

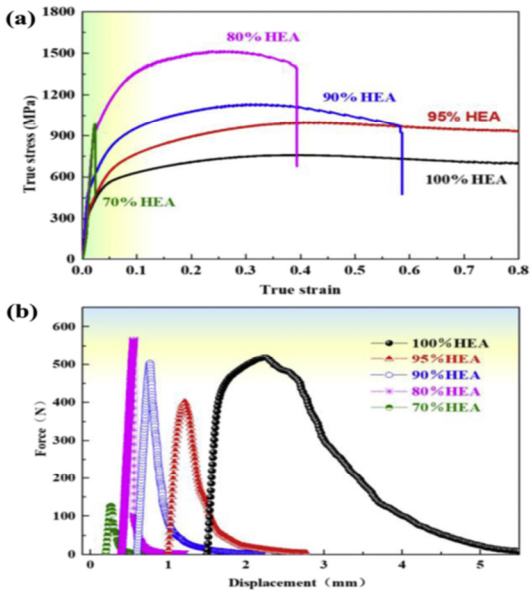

Fig. 18 True stress−strain curves of high entropy alloy composed with Fe-based metallic glass (0−30%) (a), and load−displacement curves for notched samples under three point bending (b) (Adapted with permission [30]) (Copyright 2020, Elsevier)

Table 3 provides a summary of the tensile and compressive properties presented in 3D-printed HEAC products, 3D-printed HEAs, and the casting counterparts.

Figure 19 presents the yield strength−ductility and the tensile strength−ductility relationships of the 3D-printed products of the C-HEAs, HEACs, HEAs, and casting counterparts. The 3D-printed C-HEAs had a higher yield strength (ranging from 600 to 850 MPa) followed by the 3D-printed HEAC products (ranging from 250 to 700 MPa), while the 3D-printed HEACs exhibited a higher tensile strength (ranging from 750 to 1000 MPa) followed by the 3D-printed C-HEAs (ranging from 350 to 1150 MPa) compared to the 3D-printed HEAs, and the ductility decreased in the same order. This was attributed to the addition of ceramic particles, which could act as heterogeneous nucleation points during rapid cooling and thus facilitate grain refinement and strengthen the HEA matrix, which could promote the mechanical properties of 3D-printed HEACs. In conclusion, the 3D-printed HEACs have a superior yield and tensile strength with appropriate ductility due to the combined effects of grain refinement and precipitate reinforcement.

Table 3 Tensile and compressive properties of 3D-printed HEAC products, compared with those manufactured by AM and conventional processes

HEA	Second phase	Second phase content/%	Parameter		Printing process	Tensile property			Compressive property			Ref.
			P/W	*v*/(mm·s^{-1})		YS/MPa	UTS/MPa	El/%	YS/MPa	UCS/MPa	El/%	
FeCoCrNi	C	0.05	250	800	SLM	630	776	9.6	−	−	−	[63]
			300	800		635	788	11.3	−	−	−	
			350	800		630	786	11.9	−	−	−	
			400	800		638	797	13.5	−	−	−	
			400	1000		643	789	11.5	−	−	−	
			400	1200		656	783	7.7	−	−	−	
	C	0.05	400	800	SLM	638	795	13.5	−	−	−	[64]
	C	0.05	400	800	SLM, 1073 K for 0.5 h annealing	720	905	9.7	−	−	−	[65]
					SLM, 1073 K for 8 h annealing	787	950	10	−	−	−	
$Fe_{49.5}Mn_{30}Co_{10}Cr_{10}$	C	0.5	180	1000	SLM	710	1000	28	−	−	−	[99]
CoCrFeMnNi	C	1	90	200	SLM	829	989	24.3	−	−	−	[62]
			90	600		741	874	39.7	−	−	−	
	BMG	0	185	600	SLM	−	−	−	315		80	[30]
		5				−	−	−	384		80	
		10				−	−	−	595	1150	58	
		20				−	−	−	916	1500	39	
		30				−	−	−	Broken during test			
	TiC	12	250	450	SLM	−	1100	8	−	−	−	[73]
		5	200	200−1200	SLM	−	1036	12	−	−	−	[74]
		5	375	1600	SLM	−	1059	15.3	−	−	−	[75]
		5	375	1600	RLSS−SLM	−	1100	18				[75]
	WC	5	1000	8.3	LMD, at RT	502	776	37	−	−	−	[104]
		10				675	845	9	−	−	−	
		0	1000	8.3	LMD, at 873 K	−	280	57	−	−	−	
		5				−	405	45	−	−	−	
	TiC	0	−	−	LMD	300	550	50	−	−	−	[111]
		2.5				330	610	47	−	−	−	
		5				385	723	32	−	−	−	
FeCoCrNi	−	−	200	300	SLM	402−600	480−745	8−32	−	−	−	[29]
	−	−	150	270		572	691	17.9	−	−	−	[113]
CoCrFeMnNi	−	−	400	800−4000	SLM	519	601	34	−	−	−	[114]
	−	−	160−290	1500−2500		510	609	34	−	−	−	[115]
	−	−	880	10	LAAM	518	660	19.8	−	−	−	[116]
	−	−	1000−1400	8.3	LMD	290	535	55	−	−	−	[117]
	−	−	600−1000	13.3	LAM	346	566	27	−	−	−	[118]
	−	−	350−400	6.6−10	LENS	424	651	48	−	−	−	[119]
FeCoCrNiMn	−	−	−	−		209	496	55	−	−	−	[8]
FeCoCrNi	−	−	−	−	Casting	188	457	50	−	−	−	[29]
$Fe_{49.5}Mn_{30}Co_{10}Cr_{10}C_{0.5}$	−	−	−	−		230	739	52	−	−	−	[120]

4.2 Microhardness and wear resistance

In terms of the hardness and wear resistance, 3D-printed HEAC coatings are characterized by high hardness and wear resistance. For example, the addition of NbC particles improved the microhardness and wear resistance of AlCoCrFeNi$_x$NbC HEA (x=10, 20, 30, wt.%) fabricated by laser cladding due to the fine microstructure and the solution strengthening effect. Good comprehensive mechanical properties were obtained for the HEA by adding 20 wt.% NbC particles. As shown in Fig. 20, at 20 wt.% NbC, the average Vickers hardness is HV 525 (Fig. 20(a)), the average friction coefficient is 1.023, and the mass loss is 1.05 mg (Fig. 20(b)) [76].

Additionally, FeCoCrAlCu/ZrO_2 HEACs fabricated by LMD exhibited better wear performance than FeCoCrAlCu HEA due to its additional phases, such as the quasicrystalline/nanocrystalline phases, and the compact and fine free-microcrack microstructure [106]. The wear resistance and the hardness for coatings containing Ti increased significantly [107]. At x=1, the hardness of the coating was much more than 3 times higher than that of the substrate, and its wear mass was approximately 1/3 that of the substrate. However, the hardness distribution was uneven, which may be due to the segregation and growth of TiN particles and the production of Laves phases.

4.3 Corrosion/oxidation resistance

HEACs exhibit high corrosion/oxidation resistance. For example, CNTs/UNs modified LMD composites showed better corrosion and high-temperature oxidation resistance than a TA2 alloy. As shown in Figs. 21(a, b), deep holes were formed in the corrosion zone of a TA2 substrate, exhibiting serious pitting corrosion, which was attributed to damage of the passive film generated by the Cl^- ions, while the corrosion resistance of the HEACs was better than that of the substrate. This was attributed to the production of the nanoscale ceramics and UNs, which are able to penetrate into the atomic structure of the CNTs, resulting in

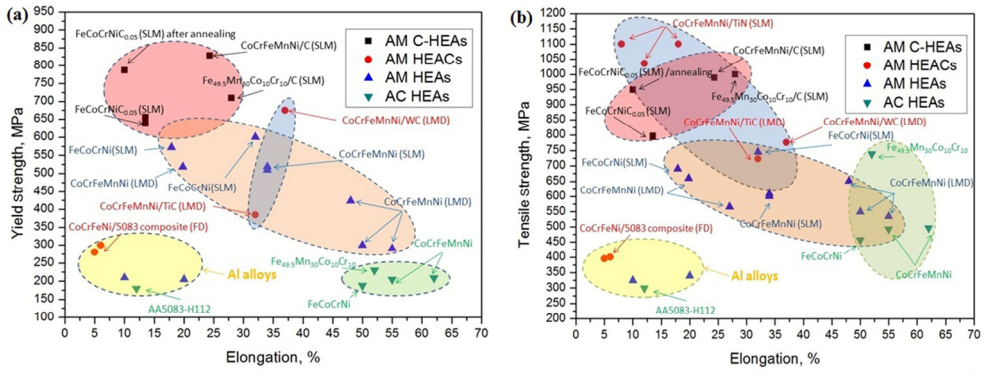

Fig. 19 Summary of yield (a) and tensile strength (b) versus elongation for HEAs products

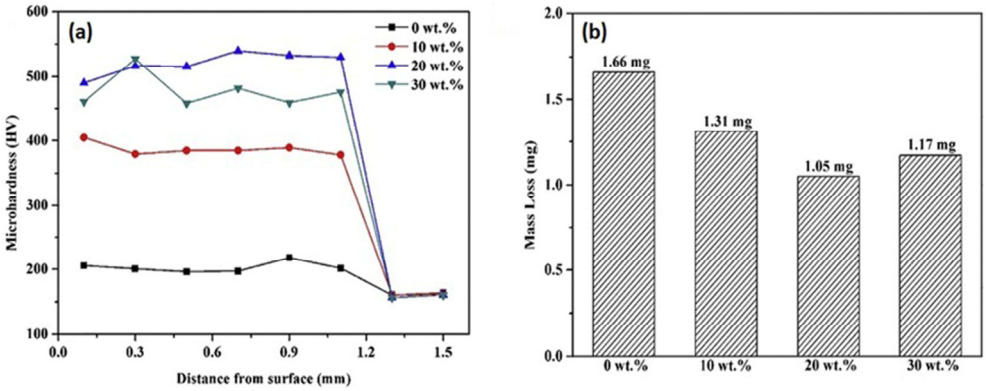

Fig. 20 Microhardness (a), and wear loss (b) of AlCoCrFeNi$_x$NbC HEAs coatings (Adapted with permission [76]) (Copyright 2019, Elsevier)

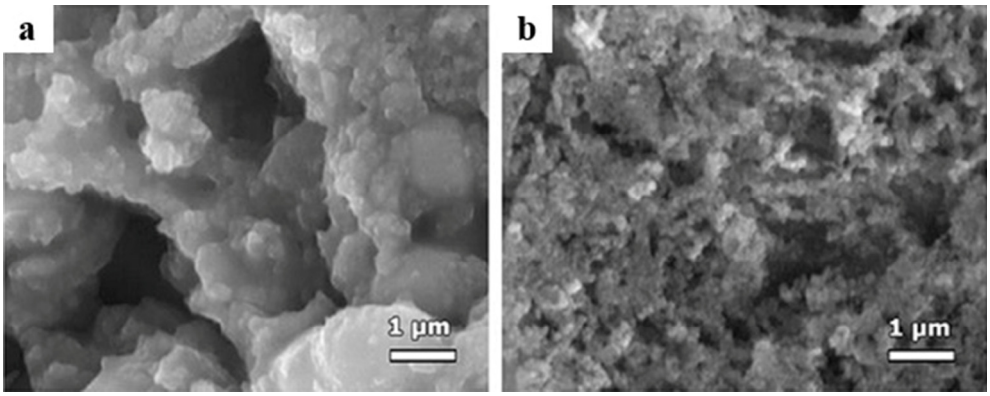

Fig. 21 Corrosion surfaces of substrate (a) and HEACs (b) (Adapted with permission [108]) (Copyright 2020, Elsevier)

dispersion strengthening and lattice distortion, thus leading to the improvement of corrosion/high-temperature oxidation resistance of HEACs [108].

5 Perspectives for future of 3D-printed HEACs

3D-printed HEACs are new composite materials that can potentially act as functional and structural materials due to their excellent properties. Therefore, our perspectives regarding the future of 3D-printed HEACs are suggested as follows:

(1) The mechanical properties of the 3D-printed HEACs at different temperatures (at cryogenic and high temperatures) should be investigated.

(2) Post-processing on these materials, and its effects on the microstructures and material properties should be studied.

(3) Most works focus on tensile and compressive strength; hence, it is essential to focus on other properties, such as fracture toughness, fatigue, creep, oxidation, and corrosion.

(4) Furthermore, most of the reported alloys are CoCrFeMnNi systems. Future work should address other HEAs, such as lightweight or refractory HEAs, which are considered challenging materials for 3D printing.

6 Conclusions

The recent achievements of 3D-printed high-entropy alloy composites (HEACs) were reviewed in terms of their powder development, printing processes, microstructures, and properties. The article begins with an introduction of the HEAs and HEA composites, and addresses the reviews published about the 3D-printed HEA products. The processes of HEAC powders development, including gas atomization and mechanical alloying, and the powder properties are presented. Gas atomization allows for the production of spherical powder particles, while mechanical alloying produces HEAC powders with homogeneous microstructures and irregularly-shaped particles. Additionally, the phases of HEACs prepared by mechanical alloying are affected by the milling parameters, such as the ball-to-powder ratio, milling time, and the rotating speed of the mill. The additive manufacturing processes of HEAC powders, such as powder bed fusion, directed energy deposition, and other processes, and their microstructures were discussed. The mechanical properties of 3D-printed HEACs are discussed and compared with those of 3D-printed HEAs and their casting counterparts. The 3D-printed HEACs have a superior yield and tensile strength with appropriate ductility, which is attributed to the fine micro-structure formed due to the addition of ceramic reinforcement particles and the rapid solidification during the fabrication process. In addition, the hardness and the resistance to wear, corrosion, and oxidation of 3D-printed HEACs are discussed. It is found that the HEAC coatings containing reinforcement ceramic particles have high wear resistance and hardness as well as corrosion/oxidation resistance. Finally, proposals are made for future research.

Acknowledgments

This work was financially supported by the National Natural Science Foundation of China

(No. 52061160483). The authors are also grateful to the Analytical and Testing Center, Huazhong University of Science and Technology, China.

References

[1] CANTOR B, CHANG I T H, KNIGHT P, VINCENT A J B. Microstructural development in equiatomic multicomponent alloys [J]. Materials Science and Engineering A, 2004, 375/376/377: 213−218.

[2] YEH J W, CHEN S K, LIN S J, GAN J Y, CHEN T S, CHEN T T, TSAU C H, CHANG S Y. Nanostructured high entropy alloys with multiple principal elements: novel alloy design concepts and outcomes [J]. Advanced Engineering Materials, 2004, 6: 299−303.

[3] YEH J W. Recent progress in high-entropy alloys [J]. Ann Chim Sci Mat, 2006, 31: 633−648.

[4] MIRACLE D B, SENKOV O N. A critical review of high entropy alloys and related concepts [J]. Acta Materialia, 2017, 122: 448−511.

[5] YEH J W. Physical metallurgy of high-entropy alloys [J]. JOM, 2015, 67: 2254−2261.

[6] ZHANG Y, ZUO T T, TANG Z, GAO M C, DAHMEN K A, LIAW P K, LU Z P. Microstructures and properties of high-entropy alloys [J]. Progress in Materials Science, 2014, 61: 1−93.

[7] ZHOU Y J, ZHANG Y, WANG Y L, CHEN G L. Solid solution alloys of $AlCoCrFeNiTi_x$ with excellent room-temperature mechanical properties [J]. Applied Physics Letters, 2007, 90: 181904.

[8] HE J Y, LIU W H, WANG H, WU Y, LIU X J, NIEH T G, LU Z P. Effects of Al addition on structural evolution and tensile properties of the FeCoNiCrMn high-entropy alloy system [J]. Acta Materialia, 2014, 62: 105−113.

[9] DONG Yong, JIANG Li, JIANG Hui, LU Yi-ping, WANG Tong-min, LI Ting-ju. Effects of annealing treatment on microstructure and hardness of bulk $AlCrFeNiMo_{0.2}$ eutectic high-entropy alloy [J]. Materials & Design, 2015, 82: 91−97.

[10] CHUANG M H, TSAI M H, WANG W R, LIN S J, YEH J W. Microstructure and wear behavior of $Al_xCo_{1.5}CrFeNi_{1.5}Ti_y$ high-entropy alloys [J]. Acta Materialia, 2011, 59: 6308−6317.

[11] HSU C Y, YEH J W, CHEN S K, SHUN T T. Wear resistance and high-temperature compression strength of FCC CuCoNiCrAl0.5Fe alloy with boron addition [J]. Metallurgical and Materials Transactions A, 2004, 35: 1465−1469.

[12] XIAO Wei-cheng, LI Kun, HAN Liu-liu, LIU Yong. Self-lubricating behavior of $Fe_{22}Co_{26}Cr_{20}Ni_{22}Ta_{10}$ high-entropy alloy matrix composites [J]. Transactions of Nonferrous Metals Society of China, 2021, 31: 744−752.

[13] HEMPHILL M A, YUAN T, WANG G Y, YEH J W, TSAI C W, CHUANG A, LIAW P K. Fatigue behavior of $Al_{0.5}CoCrCuFeNi$ high entropy alloys [J]. Acta Materialia, 2012, 60: 5723−5734.

[14] CHEN P Y, LEE C H, WANG S Y, SEIFI M, LEWANDOWSKI J J, DAHMEN K A, JIA H L, XIE X, CHEN B L, YEH J W, TSAI C W, YUAN T, LIAW P K. Fatigue behavior of high-entropy alloys: A review [J]. Science China Technological Sciences, 2018, 61: 168−178.

[15] CHOU Y L, YEH J W, SHIH H C. The effect of molybdenum on the corrosion behaviour of the high-entropy alloys $Co_{1.5}CrFeNi_{1.5}Ti_{0.5}Mo_x$ in aqueous environments [J]. Corrosion Science, 2010, 52: 2571−2581.

[16] SENKOV O N, SENKOVA S V, DIMIDUK D M, WOODWARD C, MIRACLE D B. Oxidation behavior of a refractory $NbCrMo_{0.5}Ta_{0.5}TiZr$ alloy [J]. Journal of Materials Science, 2012, 47: 6522−6534.

[17] HUANG Can, ZHANG Yong-zhong, SHEN Jian-yun, VILAR R. Thermal stability and oxidation resistance of laser clad TiVCrAlSi high entropy alloy coatings on Ti−6Al−4V alloy [J]. Surface & Coatings Technology, 2011, 206: 1389−1395.

[18] SUN S J, TIAN Y Z, LIN H R, DONG X G, WANG Y H, ZHANG Z J, ZHANG Z F. Enhanced strength and ductility of bulk CoCrFeMnNi high entropy alloy having fully recrystallized ultrafine-grained structure [J]. Materials & Design, 2017, 133: 122−127.

[19] LIU W H, WU Y, HE J Y, NIEH T G, LU Z P. Grain growth and the Hall−Petch relationship in a high-entropy FeCrNiCoMn alloy [J]. Scripta Materialia, 2013, 68: 526−529.

[20] LIU Yuan, ZHANG Yan, ZHANG Heng, WANG Nai-juan, CHEN Xiang, ZHANG Hua-wei, LI Yan-xiang. Microstructure and mechanical properties of refractory $HfMo_{0.5}NbTiV_{0.5}Si_x$ high-entropy composites [J]. Journal of Alloys and Compounds, 2017, 694: 869−876.

[21] SENKOV O N, WILKS G B, MIRACLE D B, CHUANG C P, LIAW P K. Refractory high-entropy alloys [J]. Intermetallics, 2010, 18: 1758−1765.

[22] ROGAL Ł, CZERWINSKI F, JOCHYM P T, LITYNSKA-DOBRZYNSKA L. Microstructure and mechanical properties of the novel $Hf_{25}Sc_{25}Ti_{25}Zr_{25}$ equiatomic alloy with hexagonal solid solutions [J]. Materials & Design, 2016, 92: 8−17.

[23] TRACY C L, PARK S, RITTMAN D R, ZINKLE S J, BEI H B, LANG M, EWING R C, MAO W L. High pressure synthesis of a hexagonal close-packed phase of the high-entropy alloy CrMnFeCoNi [J]. Nature Communications, 2017, 8: 15634.

[24] LU Y P, DONG Y, GUO S, JIANG L, KANG H J, WANG T M, WEN B, WANG Z J, JIE J C, CAO Z Q, RUAN H H, LI T J. A promising new class of high-temperature alloys: Eutectic high-entropy alloys [J]. Scientific Reports, 2014, 4: 6200.

[25] HE Feng, WANG Zhi-jun, CHENG Peng, WANG Qiang, LI Jun-jie, DANG Ying-ying, WANG Jin-cheng, LIU C T. Designing eutectic high entropy alloys of $CoCrFeNiNb_x$ [J]. Journal of Alloys and Compounds, 2016, 656: 284−289.

[26] OTTO F, DLOUHY A, SOMSEN C, BEI H, EGGELER G, GEORGE E P. The influences of temperature and microstructure on the tensile properties of a CoCrFeMnNi high-entropy alloy [J]. Acta Materialia, 2013, 61: 5743−5755.

[27] GLUDOVATZ B, HOHENWARTER A, CATOOR D, CHANG E H, GEORGE E P, RITCHIE R O. A fracture-resistant high-entropy alloy for cryogenic applications [J]. Science, 2014, 345: 1153−1158.

[28] TONG Y, CHEN D, HAN B, WANG J, FENG R, YANG T, ZHAO C, ZHAO Y L, GUO W, SHIMIZU Y, LIU C T, LIAW P K, INOUE K, NAGAI Y, HU A, KAI J J. Outstanding tensile properties of a precipitation-strengthened

$FeCoNiCrTi_{0.2}$ high-entropy alloy at room and cryogenic temperatures [J]. Acta Materialia, 2019: 228−240.

[29] BRIF Y, THOMAS M, TODD I. The use of high-entropy alloys in additive manufacturing [J]. Scripta Materialia, 2015, 99: 93−96.

[30] LI Ning, WU Shi-xing, OUYANG Di, ZHANG Jian-ji, LIU Lin. Fe-based metallic glass reinforced FeCoCrNiMn high entropy alloy through selective laser melting [J]. Journal of Alloys and Compounds, 2020, 822: 153695.

[31] WANG Zhang-wei, WU M, CAI Zhong-hou, CHEN Si, BAKER I. Effect of Ti content on the microstructure and mechanical behavior of $(Fe_{36}Ni_{18}Mn_{33}Al_{13})_{100-x}Ti_x$ high entropy alloys [J]. Intermetallics, 2016, 75: 79−87.

[32] SATYANARAYANA P V, SOKKALINGAM R, JENA P K, SIVAPRASAD K, PRASHANTH K G. Tungsten matrix composite reinforced with CoCrFeMnNi high-entropy alloy: Impact of processing routes on microstructure and mechanical properties [J]. Metals, 2019, 9: 992.

[33] GUO Zhi-ming, ZHANG Ai-jun, HAN Jie-sheng, MENG Ju-hu. Effect of Si additions on microstructure and mechanical properties of refractory NbTaWMo high-entropy alloys [J]. Journal of Materials Science, 2019, 54: 5844−5851.

[34] QIN Gang, CHEN Rui-run, ZHENG Hui-ting, FANG Hong-ze, WANG Liang, SU Yan-qing, GUO Jing-jie, FU Heng-zhi. Strengthening FCC-CoCrFeMnNi high entropy alloys by Mo addition [J]. Journal of Materials Science & Technology, 2019, 35: 578−583.

[35] XIAN Xin, LIN Li-jing, ZHONG Zhi-hong, ZHANG Chao, CHEN Chang, SONG Kui-jing, CHENG Ji-gui, WU Yu-cheng. Precipitation and its strengthening of Cu-rich phase in $CrMnFeCoNiCu_x$ high-entropy alloys [J]. Materials Science and Engineering A, 2018, 713: 134−140.

[36] QIN Gang, WANG Shu, CHEN Rui-run, ZHENG Hui-ting, WANG Liang, SU Yan-qing, GUO Jing-jie, FU Heng-zhi. Improvement of microstructure and mechanical properties of CoCrCuFeNi high-entropy alloys by V addition [J]. Journal of Materials Engineering and Performance, 2019, 28: 1049−1056.

[37] LIU W H, HE J Y, HUANG H L, WANG H, LU Z P, LIU C T. Effects of Nb additions on the microstructure and mechanical property of CoCrFeNi high-entropy alloys [J]. Intermetallics, 2015, 60: 1−8.

[38] JIANG Hui, JIANG Li, QIAO Dong-xu, LU Yi-ping, WANG Tong-min, CAO Zhi-qiang, LI Ting-ju. Effect of niobium on microstructure and properties of the $CoCrFeNb_xNi$ high entropy alloys [J]. Journal of Materials Science & Technology, 2017, 33: 712−717.

[39] FENG Jun-jie, GAO Shuo, HAN Kun, MIAO Yi-dong, QI Ji-qiu, WEI Fu-xiang, REN Yao-jian, ZHAN Zhen-zhen, SUI Yan-wei, SUN Zhi, CAO Peng. Effects of minor B addition on microstructure and properties of $Al_{19}Co_{20}Fe_{20}Ni_{41}$ eutectic high-entropy alloy [J]. Transactions of Nonferrous Metals Society of China, 2021, 31: 1049−1058.

[40] ROGAL Ł, KALITA D, TARASEK A, BOBROWSKI P, CZERWINSKI F. Effect of SiC nano-particles on microstructure and mechanical properties of the CoCrFeMnNi high entropy alloy [J]. Journal of Alloys and Compounds, 2017, 708: 344−352.

[41] WANG Gang, YANG Yun-long, HE Ru-jie, TAN Cai-wang, HUTTULA M, CAO Wei. A novel high entropy CoFeCrNiCu alloy filler to braze SiC ceramics [J]. Journal of the European Ceramic Society, 2020, 40: 3391−3398.

[42] FAN Q C, LI B S, ZHANG Y. The microstructure and properties of $(FeCrNiCo)Al_xCu_y$ high-entropy alloys and their TiC-reinforced composites [J]. Materials Science and Engineering A, 2014, 598: 244−250.

[43] CHENG Hu, CHEN Wei, LIU Xiao-qiang, TANG Qun-hua, XIE Yan-chong, DAI Pin-qiang. Effect of Ti and C additions on the microstructure and mechanical properties of the FeCoCrNiMn high-entropy alloy [J]. Materials Science and Engineering A, 2018, 719: 192−198.

[44] YIM D M, SATHIYAMOORTHI P, HONG S J, KIM H S. Fabrication and mechanical properties of TiC reinforced CoCrFeMnNi high-entropy alloy composite by water atomization and spark plasma sintering [J]. Journal of Alloys and Compounds, 2019, 781: 389−396.

[45] WANG Jian-ying, FANG Jing-hua, YANG Hai-lin, LIU Zhi-lin, LI Rui-di, JI Shou-xun, WANG Yun, RUAN Jian-ming. Mechanical properties and wear resistance of medium entropy $Fe_{40}Mn_{40}Cr_{10}Co_{10}$/TiC composites [J]. Transactions of Nonferrous Metals Society of China, 2019, 29: 1484−1494.

[46] ROGAL Ł, KALITA D, LIDIA L D. CoCrFeMnNi high entropy alloy matrix nanocomposite with addition of Al_2O_3 [J]. Intermetallics, 2017, 86: 104−109.

[47] YANG Shao-feng, ZHANG Yan, YAN Xing, ZHOU Hang, PI Jin-hong, ZHU De-zhi. Deformation twins and interface characteristics of nano-Al_2O_3 reinforced $Al_{0.4}FeCr-Co_{1.5}NiTi_{0.3}$ high entropy alloy composites [J]. Materials Chemistry and Physics, 2018, 210: 240−244.

[48] BIKAS H, STAVROPOULOS P, CHRYSSOLOURIS G. Additive manufacturing methods and modelling approaches: A critical review [J]. The International Journal of Advanced Manufacturing Technology, 2016, 83: 389−405.

[49] MICHAEL M H. Overview of additive manufacturing process [C]//ZHANG J, JUNG Y G. Additive Manufacturing. Cambridge, MA: USA: Butterworth-Heinemann, 2018: 1−38.

[50] CUI Wen-yuan, ZHANG Xin-chang, LIOU F. Additive manufacturing of high-entropy alloys — A review [C]// Proceedings of the 28th Annual International Solid Freeform Fabrication Symposium – An Additive Manufacturing Conference. Austin, TX, 2017: 712−724.

[51] CHEN Shu-ying, TONG Yang, LIAW P K. Additive manufacturing of high-entropy alloys: A review [J]. Entropy, 2018, 20: 937.

[52] TORRALBA J M, CAMPOS M. High entropy alloys manufactured by additive manufacturing [J]. Metals, 2020, 10: 639.

[53] HAN Chang-jun, FANG Qi-hong, SHI Yu-sheng, TOR S B, CHUA C K, ZHOU Kun. Recent advances on high-entropy alloys for 3D printing [J]. Advanced Materials, 2020, 32: e1903855.

[54] KIM J, WAKAI A, MORIDI A. Materials and manufacturing renaissance: Additive manufacturing of high-entropy alloys [J]. Journal of Materials Research, 2020, 35: 1963−1983.

[55] ZHANG Chen, ZHU Jun-kai, ZHENG Huai, LI Hui, LIU Sheng, CHENG G J. A review on microstructures and properties of high entropy alloys manufactured by selective laser melting [J]. International Journal of Extreme Manufacturing, 2020, 2: 032003.

[56] ALSHATAIF Y, SIVASANKARAN S, AL-MUFADI F A, ALABOODI A S, AMMAR H R. Manufacturing methods, microstructural and mechanical properties evolutions of high entropy alloys: A review [J]. Metals and Materials International, 2020, 26: 1099−1133.

[57] GORSSE S, HUTCHINSON C, GOUNÉ M, BANERJEE R. Additive manufacturing of metals: A brief review of the characteristic microstructures and properties of steels, Ti−6Al−4V and high-entropy alloys [J]. Science and Technology of Advanced Materials, 2017, 18: 584−610.

[58] MOSTAFAEI A, HUGHES E T, HILLA C, STEVENS E L, CHMIELUS M. Data on the densification during sintering of binder jet printed samples made from water-and gas-atomized alloy 625 powders [J]. Data in Brief, 2017, 10: 116−121.

[59] MOSTAFAEI A, TOMAN J, STEVENS E L, HUGHES E T, KRIMER Y L, CHMIELUS M. Microstructural evolution and mechanical properties of differently heat-treated binder jet printed samples from gas- and water-atomized alloy 625 powders [J]. Acta Materialia, 2017, 124: 280−289.

[60] ZHANG Lin, CHEN Xiao-wei, LI Dan, CHEN Chi, QU Xuan-hui, HE Xin-bo, LI Zhou. A comparative investigation on MIM418 superalloy fabricated using gas- and water-atomized powders [J]. Powder Technology, 2015, 286: 798−806.

[61] SI Chao-run, TANG Xing-ling, ZHANG Xian-jie, WANG Jun-biao, WU Wei-chao. Characteristics of 7055Al alloy powders manufactured by gas-solid two-phase atomization: A comparison with gas atomization process [J]. Materials & Design, 2017, 118: 66−74.

[62] PARK J M, CHOE J H, KIM J G, BAE J W, MOON J, YANG S S, KIM K T, YU J H, KIM H S. Superior tensile properties of 1%C−CoCrFeMnNi high-entropy alloy additively manufactured by selective laser melting [J]. Materials Research Letters, 2020, 8: 1−7.

[63] ZHOU Rui, LIU Yong, ZHOU Cheng-shang, LI Si-qin, WU Wen-qian, SONG Min, LIU Bin, LIANG Xiao-peng, LIAW P K. Microstructures and mechanical properties of C-containing FeCoCrNi high entropy alloy fabricated by selective laser melting [J]. Intermetallics, 2018, 94:165−171.

[64] WU Wen-qian, ZHOU Rui, WEI Bing-qiang, NI Song, LIU Yong, SONG Min. Nanosized precipitates and dislocation networks reinforced C-containing CoCrFeNi high-entropy alloy fabricated by selective laser melting [J]. Materials Characterization, 2018, 144: 605−610.

[65] ZHOU Rui, LIU Yong, LIU Bin, LI Jia, FANG Qi-hong. Precipitation behavior of selective laser melted FeCoCrNi-C0.05 high entropy alloy [J]. Intermetallics, 2019, 106: 20−25.

[66] CHAWLA V, PRAKASH S, SIDHU B S. State of the art: Applications of mechanically alloyed nanomaterials — A review [J]. Materials and Manufacturing Processes, 2007, 22: 469−473.

[67] GU Dong-dong, WANG Zhi-yang, SHEN Yifu, LI Qin, LI Yu-fang. In-situ TiC particle reinforced Ti−Al matrix composites: Powder preparation by mechanical alloying and selective laser melting behavior [J]. Applied Surface Science, 2009, 255: 9230−9240.

[68] WANG Hong-qiao, GU Dong-dong. Nanometric TiC reinforced $AlSi_{10}Mg$ nanocomposites: Powder preparation by high-energy ball milling and consolidation by selective laser melting [J]. Journal of Composite Materials, 2015, 49: 1639−1651.

[69] SURYANARAYANA C. Mechanical alloying and milling [J]. Progress in Materials Science, 2001, 46: 1−184.

[70] SURYANARAYANA C, AL-AQEELI N. Mechanically alloyed nanocomposites [J]. Progress in Materials Science, 2013, 58: 383−502.

[71] ZHU Tie, WU Hong, ZHOU Rui, ZHANG Ning-yi, YIN Yong, LIANG Lu-xin, LIU Yong, LI Jia, SHAN Quan, LI Qing-xian, HUANG Wei-dong. Microstructures and tribological properties of TiC reinforced FeCoNiCuAl high-entropy alloy at normal and elevated temperature [J]. Metals, 2020, 10: 387.

[72] CHEN C S, YANG C C, CHAI H Y, YEH J W, CHAU J L H. Novel cermet material of WC/multi-element alloy [J]. International Journal of Refractory Metals and Hard Materials, 2014, 43: 200−204.

[73] LI Bo, QIAN Bo, XU Yi, LIU Zhi-yuan, XUAN Fu-zhen. Fine-structured CoCrFeNiMn high-entropy alloy matrix composite with 12 wt.% TiN particle reinforcements via selective laser melting assisted additive manufacturing [J]. Materials Letters, 2019, 252: 88−91.

[74] LI Bo, ZHANG Lei, XU Yi, LIU Zhi-yuan, QIAN Bo, XUAN Fu-zhen. Selective laser melting of CoCrFeNiMn high entropy alloy powder modified with nano-TiN particles for additive manufacturing and strength enhancement: Process, particle behavior and effects [J]. Powder Technology, 2020, 360: 509−521.

[75] LI Bo, ZHANG Lei, YANG Bin. Grain refinement and localized amorphization of additively manufactured high-entropy alloy matrix composites reinforced by nano ceramic particles via selective-laser-melting/remelting [J]. Composites Communications, 2020, 19: 56−60.

[76] LI Xiao-feng, FENG Ying-hao, LIU Bin, YI Deng-hao, YANG Xiao-hui, ZHANG Wei-dong, CHEN Gang, LIU Yong, BAI Pei-kang. Influence of NbC particles on microstructure and mechanical properties of AlCoCrFeNi high-entropy alloy coatings prepared by laser cladding [J]. Journal of Alloys and Compounds, 2019, 788: 485−494.

[77] KOK Y, TAN X P, WANG P, NAI M L S, LOH N H, LIU E, TOR S B. Anisotropy and heterogeneity of microstructure and mechanical properties in metal additive manufacturing: A critical review [J]. Materials & Design, 2018, 139: 565−586.

[78] ASTM International. Standard terminology for additive manufacturing technologies [S]. West Conshohocken, PA: ASTM International, 2010.

[79] ZHAO Shu-ming, SHEN Xian-feng, YANG Jia-lin, TENG Wen-hua, WANG Ying-ying. Densification behavior and mechanical properties of nanocrystalline TiC reinforced 316L stainless steel composite parts fabricated by selective laser melting [J]. Optics & Laser Technology, 2018, 103: 239−250.

[80] NEMATOLLAHI M, JAHADAKBAR A, MAHTABI M J, ELAHINIA M. Additive manufacturing (AM) [M]//Metals for Biomedical Devices. 2nd ed. Sawston, Cambridge, UK: Woodhead Publishing Series in Biomaterials, 2019: 331−353.

[81] GU D D, MEINERS W, WISSENBACH K, POPRAWE R. Laser additive manufacturing of metallic components: materials, processes and mechanisms [J]. International

Materials Reviews, 2012, 57: 133−164.
[82] LIU Shun-yu, SHIN Y C. Additive manufacturing of Ti_6Al_4V alloy: A review [J]. Materials & Design, 2019, 164: 107552.
[83] ZHANG Hui, PAN Ye, HE Yi-zhu, WU Ji-li, YUE T M, GUO Sheng. Application prospects and microstructural features in laser-induced rapidly solidified high-entropy alloys [J]. JOM, 2014, 66: 2057−2066.
[84] KARTHIK G M, PANIKAR S, RAM G D J, KOTTADA R S. Additive manufacturing of an aluminum matrix composite reinforced with nanocrystalline high-entropy alloy particles [J]. Materials Science and Engineering A, 2017, 679: 193−203.
[85] ZHANG Xuan, YAO Jia-hao, LIU Bin, YAN Jun, LU Lei, LI Yi, GAO Hua-jian, LI Xiao-yan. Three-dimensional high-entropy alloy-polymer composite nanolattices that overcome the strength-recoverability trade-off [J]. Nano Letters, 2018, 18: 4247−4256.
[86] KENEL C, CASATI N P M, DUNAND D C. 3D ink-extrusion additive manufacturing of CoCrFeNi high-entropy alloy micro-lattices [J]. Nature Communications, 2019, 10: 904.
[87] MENG Guang-hui, YUE T M, LIN Xin, YANG Hai-ou, XIE Hui, DING Xu. Laser surface forming of AlCoCrCuFeNi particle reinforced AZ91D matrix composites [J]. Optics & Laser Technology, 2015, 70: 119−127.
[88] LI Jun-chen, LI Yu-long, WANG Fei-fan, MENG Xiang-chen, WAN Long, DONG Zhi-bo, HUANG Yong-xian. Friction stir processing of high-entropy alloy reinforced aluminum matrix composites for mechanical properties enhancement [J]. Materials Science and Engineering A, 2020, 792: 139755.
[89] CHEN Jian, YAO Zhi-hao, WANG Xiao-bo, LU Yu-kun, WANG Xian-hui, LIU Yong, FAN Xin-hui. Effect of C content on microstructure and tensile properties of as-cast CoCrFeMnNi high entropy alloy [J]. Materials Chemistry and Physics, 2018, 210: 136−145.
[90] XIE Yan-chong, CHENG Hu, TANG Qun-hua, CHEN Wei, CHEN Wei-kun, DAI Pin-qiang. Effects of N addition on microstructure and mechanical properties of CoCrFeNiMn high entropy alloy produced by mechanical alloying and vacuum hot pressing sintering [J]. Intermetallics, 2018, 93: 228−234.
[91] WANG Zhang-wei, BAKER I, CAI Zhong-hou, CHEN Si, POPLAWSKY J D, GUO Wei. The effect of interstitial carbon on the mechanical properties and dislocation substructure evolution in $Fe_{40.4}Ni_{11.3}Mn_{34.8}Al_{7.5}Cr_6$ high entropy alloys [J]. Acta Materialia, 2016, 120: 228−239.
[92] FAN J T, ZHANG L J, YU P F, ZHANG M D, LIU D J, ZHOU Z, CUI P, MA M Z, JING Q, LI G, LIU R P. Improved the microstructure and mechanical properties of AlFeCoNi high-entropy alloy by carbon addition [J]. Materials Science and Engineering A, 2018, 728: 30−39.
[93] GUO N N, WANG L, LUO L S, LI X Z, CHEN R R, SU Y Q, GUO J J, FU H Z. Microstructure and mechanical properties of in-situ MC-carbide particulates-reinforced refractory high-entropy Mo0.5NbHf0.5ZrTi matrix alloy composite [J]. Intermetallics, 2016, 69: 74−77.
[94] LI Zhi-ming. Interstitial equiatomic CoCrFeMnNi high-entropy alloys: carbon content, microstructure, and compositional homogeneity effects on deformation behavior [J]. Acta Materialia, 2019, 164: 400−412.
[95] EMAMIFAR A, SADEGHI B, CAVALIERE P, ZIAEI H. Microstructural evolution and mechanical properties of AlCrFeNiCoC high entropy alloy produced via spark plasma sintering [J]. Powder Metallurgy, 2019, 62: 61−70.
[96] STEPANOV N D, YURCHENKO N Y, TIKHONOVSKY M A, SALISHCHEV G A. Effect of carbon content and annealing on structure and hardness of the CoCrFeNiMn-based high entropy alloys [J]. Journal of Alloys and Compounds, 2016, 687: 59−71.
[97] ZHANG Lin, SONG Ruo-kang, QU Guo-xin, LU Tong. Effect of nitrogen on microstructure and mechanical properties of CrMnFeVTi6 high entropy alloy [J]. Transactions of Nonferrous Metals Society of China, 2021, 31: 2415−2427.
[98] LIU Bin, WANG Jing-shi, LIU Yong, FANG Qi-hong, WU Yuan, CHEN Shi-qi, LIU C T. Microstructure and mechanical properties of equimolar FeCoCrNi high entropy alloy prepared via powder extrusion [J]. Intermetallics, 2016, 75: 25−30.
[99] ZHU Z G, AN X H, LU W J, LI Z M, NG F L, LIAO X Z, RAMAMURTY U, NAI S M L, WEI J. Selective laser melting enabling the hierarchically heterogeneous microstructure and excellent mechanical properties in an interstitial solute strengthened high entropy alloy [J]. Materials Research Letters, 2019, 7: 453−459.
[100] ZHAO X, WEI Q S, GAO N, ZHENG E L, SHI Y S, YANG S F. Rapid fabrication of TiN/AISI 420 stainless steel composite by selective laser melting additive manufacturing [J]. Journal of Materials Processing Technology, 2019, 270: 8−19.
[101] LI Xiao-peng. Additive manufacturing of advanced multi-component alloys: Bulk metallic glasses and high entropy alloys [J]. Advanced Engineering Materials, 2018, 20: 1700874.
[102] CHEN Jian, NIU Peng-yun, WEI Ting, HAO Liang, LIU Yun-zi, WANG Xian-hui, PENG Yu-li. Fabrication and mechanical properties of AlCoNiCrFe high-entropy alloy particle reinforced Cu matrix composites [J]. Journal of Alloys and Compounds, 2015, 649: 630−634.
[103] LI Chen-wei, CHANG Kai-chun, YEH An-chou. On the microstructure and properties of an advanced cemented carbide system processed by selective laser melting [J]. Journal of Alloys and Compounds, 2019, 782: 440−450.
[104] LI Jin-feng, XIANG Shuo, LUAN Heng-wei, AMAR A, LIU Xue, LU Si-yuan, ZENG Yang-yang, LE Guo-min, WANG Xiao-ying, QU Feng-sheng, JIANG Chun-li, YANG Guan-nan. Additive manufacturing of high-strength CrMnFeCoNi high-entropy alloys-based composites with WC addition [J]. Journal of Materials Science & Technology, 2019, 35: 2430−2434.
[105] WELK B A, GIBSON M A, FRASER H L. A combinatorial approach to the investigation of metal systems that form both bulk metallic glasses and high entropy alloys [J]. JOM, 2016, 68: 1021−1026.
[106] LI Jia-ning, CRAEGHS W, JING Cai-nian, GONG Shui-li, SHAN Fei-hu. Microstructure and physical performance of laser-induction nanocrystals modified high-entropy alloy composites on titanium alloy [J]. Materials & Design, 2017, 117: 363−370.
[107] GUO Ya-xiong, SHANG Xiao-juan, LIU Qi-bin. Micro-structure and properties of in-situ TiN reinforced laser

cladding $CoCr_2FeNiTi_x$ high-entropy alloy composite coatings [J]. Surface and Coatings Technology, 2018, 344: 353−358.
[108] LI Jia-ning, SU Mo-lin, LI Guan-chao, LIU Li-qiang. Atomic structure revolution and excellent performance improvement of composites induced by laser ultrafine-nano technology [J]. Composites Part B: Engineering, 2020, 185: 107792.
[109] LI Jia-ning, YE Zhi-yun, FU Jin, QI Wen-jun, TIAN Yan, LIU Li-qiang, WANG Xiao-lin. Microstructure evolution, texture and laser surface HEACs of Al−Mg−Si alloy for light automobile parts [J]. Materials Characterization, 2020, 160: 110093.
[110] DAS K, BANDYOPADHYAY T K, DAS S. A review on the various synthesis routes of TiC reinforced ferrous based composites [J]. Journal of Materials Science, 2002, 37: 3881−3892.
[111] AMAR A, LI Jin-feng, XIANG Shuo, LIU Xue, ZHOU Yu-zhao, LE Guo-min, WANG Xiao-ying, QU Feng-sheng, MA Shi-yu, DONG Wu-mei, LI Qiang. Additive manufacturing of high-strength CrMnFeCoNi-based high entropy alloys with TiC addition [J]. Intermetallics, 2019, 109: 162−166.
[112] KARTHIK G M, RAM G D J, KOTTADA R S. Friction deposition of titanium particle reinforced aluminum matrix composites [J]. Materials Science and Engineering A, 2016, 653: 71−83.
[113] SUN Z, TAN X P, DESCOINS M, MANGELINCK D, TOR S B, LIM C S. Revealing hot tearing mechanism for an additively manufactured high-entropy alloy via selective laser melting [J]. Scripta Materialia, 2019, 168: 129−133.
[114] LI Rui-di, NIU Peng-da, YUAN Tie-chui, CAO Peng, CHEN Chao, ZHOU Ke-chao. Selective laser melting of an equiatomic CoCrFeMnNi high-entropy alloy: Processability, non-equilibrium microstructure and mechanical property [J]. Journal of Alloys and Compounds, 2018, 746: 125−134.
[115] ZHU Z G, NGUYEN Q B, NG F L, AN X H, LIAO X Z, LIAW P K, NAI S M L, WEI J. Hierarchical microstructure and strengthening mechanisms of a CoCrFeNiMn high entropy alloy additively manufactured by selective laser melting [J]. Scripta Materialia, 2018, 154: 20−24.
[116] CHEW Y, BI G J, ZHU Z G, NG F L, WENG F, LIU S B, NAI S M L, LEE B Y. Microstructure and enhanced strength of laser aided additive manufactured CoCrFeNiMn high entropy alloy [J]. Materials Science and Engineering A, 2019, 744: 137−144.
[117] XIANG Shuo, LUAN Heng-wei, WU Jian, YAO Ke-fu, LI Jin-feng, LIU Xue, TIAN Yan-zhong, MAO Wen-lue, BAI Hua, LE Guo-min, LI Qiang. Microstructures and mechanical properties of CrMnFeCoNi high entropy alloys fabricated using laser metal deposition technique [J]. Journal of Alloys and Compounds, 2019, 773: 387−392.
[118] TONG Zhao-peng, REN Xu-dong, JIAO Jia-fei, ZHOU Wang-fan, REN Yun-peng, YE Yun-xia, LARSON E A, GU Jia-yang. Laser additive manufacturing of FeCrCoMnNi high-entropy alloy: Effect of heat treatment on microstructure, residual stress and mechanical property [J]. Journal of Alloys and Compounds, 2019, 785: 1144−1159.
[119] MELIA M A, CARROLL J D, WHETTEN S R, ESMAEELY S N, LOCKE J, WHITE E, ANDERSON I, CHANDROSS M, MICHAEL J R, ARGIBAY N, SCHINDELHOLZ E J, KUSTAS A B. Mechanical and corrosion properties of additively manufactured CoCrFeMnNi high entropy alloy [J]. Additive Manufacturing, 2019, 29: 100833.
[120] LI Zhi-ming, TASAN C C, SPRINGER H, GAULT B, RAABE D. Interstitial atoms enable joint twinning and transformation induced plasticity in strong and ductile high-entropy alloys [J]. Scientific Reports, 2017, 7: 40704.

增材制造高熵合金复合材料综述

Hamza OSMAN[1,2]，柳 林[1]

1. 华中科技大学 材料科学与工程学院 材料成型与模具技术国家重点实验室，武汉 430074；
2. Department of Mining and Petroleum, Faculty of Engineering, Al Azhar University, Qena, Egypt

摘 要：高熵合金复合材料是一种由高熵合金基体和第二相(如碳化物、硼化物、氮化物)组成的新型金属基复合材料。近年来，高熵合金复合材料的优异性能吸引了大量研究者的关注。然而，在传统铸造高熵合金复合材料中会发生严重的成分偏析，这极大制约了高熵合金复合材料的发展。目前，新兴的 3D 打印技术可以解决这一问题并制备出复杂形状的零件，因此，得到了研究者的关注并有大量相关文献报导。本文总结了截止目前 3D 打印高熵合金复合材料的研究进展。首先，对高熵合金及其复合材料做了介绍，并总结了目前高熵合金复合材料粉末的制备方法(气雾化法和机械合金化法)。其次，介绍了几种常用于成形高熵合金复合材料的 3D 打印方法(粉末床熔化法和直接金属沉积技术)，并对其相应的微观结构进行了分析。然后，对比了 3D 打印高熵合金复合材料、3D 打印高熵合金及其铸件的力学性能，并对其硬度抗磨损、腐蚀和氧化性能进行了探讨。最后，对 3D 打印高熵合金复合材料的发展前景进行了展望。

关键词：高熵合金；复合材料；增材制造；增强相；微观结构；力学性能

(Edited by Bing YANG)